April 2010

Evaluation and Application of a High-Resolution Fiber-Optic Strain Sensor

Felicia Nicole White
Worcester Polytechnic Institute

Jacob S. Lemay
Worcester Polytechnic Institute

Michael Jay Zervas
Worcester Polytechnic Institute

Project Number : ME-CF-FO10

EVALUATION AND APPLICATION OF A HIGH-RESOLUTION FIBER-OPTIC STRAIN SENSOR

A Major Qualifying Project Report

Submitted to the Faculty

of the

WORCESTER POLYTECHNIC INSTITUTE

in partial fulfillment of the requirements for the

Degree of Bachelor of Science

in Mechanical Engineering

by

_____

Jacob Lemay

_____

Felicia White

_____

Michael Zervas

Date: 29 April, 2010

Keywords:

1 Fiber-Optic Sensor

2 Interferometery

3 Fabry-Perot Interferometer

_____

Professor Cosme Furlong

Abstract

In this project, we evaluated the measuring capabilities of a high-resolution fiber-optic strain sensor based on a miniaturized Fabry-Perot interferometer. We designed an opto-electromechanical setup to experimentally evaluate our theoretical analyses of the sensor and to verify its reliability. High-resolutions are needed for testing performance and verification of new designs, especially in electro-mechanical components. As a consequence, high resolution sensors are needed. These sensors must not alter design intent and must be immune to electromagnetic interference. Calibration was done on a cantilever beam subjected to static and dynamics loading conditions, using off the shelf electrical components. Results indicate a gage factor on the order of 40 (mV/με). These results prove the capabilities of the fiber Fabry-Perot interferometer for high-resolution measurements of strain. The fiber Fabry-Perot can be embedded into a component without significantly altering its properties as characteristic dimensions of this fiber are smaller than 125 micrometers. We also applied the sensor to study dynamics of a scaled model of a wind turbine blade. The fiber Fabry-Perot interferometer has been proven to provide high-resolution measurements in conditions where conventional strain sensors may fail to provide reliable results.

Acknowledgements

Our group owes many thanks for the generosity and support of many different individuals who helped us achieve our goals. Without them, the Evaluation and Application of a High-Resolution Fiber Optic Strain Sensor project could not have become a reality. First and foremost, we would like to graciously thank our advisor, Professor Cosme Furlong for all his support and guidance throughout this project. He provided us with helpful advice and direction as well as the opportunity to work with state-of-the-art technologies in the CHSLT Lab. His researchers in the lab were always willing to help us with any problems we encountered and they deserve to be recognized for their contribution to this project.

Our group would also like to thank the faculty members at WPI who were willing to help us achieve specific project objectives. Professor Hefti aided our group in the holographic experiments of our project and without him those experiments would not have been a success. Finally, Dr. Flores and Nikhil Bapat guided us throughout our project when advice was needed and allowed us to accomplish our goals.

In closing, our group would like to thank Worcester Polytechnic Institute for providing us with an opportunity to partake in such a wonderful project experience.

Table of Contents

Table of Figures

1 Introduction

As technology advances, new designs and components require higher resolutions for monitoring health and structural characteristics and testing their performance. The quality of new devices directly relies on the level at which you can measure their performance. Conventional techniques do not provide the high resolutions needed for new and advancing designs for measurements of different quantities, particularly strain. Classic foil strain gauges and accelerometers have been used and trusted for several years to measure strains on various structures including buildings, wind turbines, air planes and the human body, among others; however, are known to fail under harsh conditions.

We chose to work with a fiber optic strain sensor because it would not fail where a conventional strain sensor might, it has superior resolution and would not alter design intent. Fiber optic sensors are not only immune to electromagnetic interference, but can survive high temperatures and harsh weather conditions. The gauge factor of a fiber optic sensor is also significantly improved. When compared to a foil strain gauge, the gauge factor is nearly 25 times better. In our research, we chose to focus on two fiber optic strain sensors whose mechanical and optical properties changed with an applied strain – the Fiber Bragg Grating and the Fiber Fabry-Perot interferometer. From these two technologies, we chose to purchase a Fiber Fabry-Perot interferometer (FPI) from FISOs Technologies, Incorporated. The sensor was affordable and available within four weeks of our request.

Therefore the objectives of this project were as follows. To investigate the principles of operation of fiber optics for measurements of strain, to apply the sensor for measurements of strain and vibrations in specific components, and the main goal, to identify and evaluate a specific strain sensor, the FPI, by application of analytical, computation and experimental

techniques. We would like to prove the high resolution of the fiber optic strain sensor through resolution results obtained through calibration of the system as well as comparison of dynamic results from the sensor to other high resolution systems.

2 Background

In order to fully recognize the motivation of this project, information on sensing applications including structural, health and performance monitoring is needed. Conventional strain sensors such as foil strain gauges and accelerometers have been used for these applications in the past; however, fiber optics have proven and continue to prove their superiority to these sensors in several applications.

2.1 Sensing Applications

2.1.1 Structural monitoring

An overall deterioration of the United State's civil infrastructure has been brought to the attention of engineers and researchers over the past decade. As a result, new technologies, such as fiber optic sensors, have been considered to monitor large structures to avoid these failures. A nondestructive and reliable sensor is needed to perform and evaluation of the structural health of concrete and other building materials. Fiber optic sensors (FOS) have many advantages that conventional sensors such as the foil strain gauge and accelerometer do not have. FOS are extremely small, on the order of micrometers in diameter, and will not affect the material properties of the concrete or other material in which they are embedded (Merzbacher, Kersey, & Friebele, 1995). When used to test or verify smaller components, the FOS will also not alter design intent allowing for a true measurement to be taken. Other advantages include their immunity to electromagnetic interferences (EMI) which becomes particularly important when monitoring structures in lightening storms as well as small electrical components (Merzbacher, Kersey, & Friebele, 1995). Fiber optic sensors are made such that their optical and mechanical properties change with the application of some induced strain, temperature change or pressure

change, among others. These changes cause a measurable change in several parameters of the output beam of light including intensity, frequency, polarization, and phase of the lightwave. These parameters allow for fiber optic sensors to be customized for a specific task such as measuring variation in strain of the structure.

Over the past few decades the uses for fiber optic sensors has broadened significantly. To prove this, students from the University of Vermont placed FOS in a variety of structures, including highway, pedestrian, and railway bridges, a dam, and a five-story building (Huston, Ambrose, & Barker, 1994). These studies are crucial in developing better strategies for utilizing various FOS in a wide range of structures. This is important because it is ideal to embed the sensor into the structure during construction and the logistical challenges need to be solved before completion of the structure. This played a role in our project when determining the placement of the sensor within the two scaled structures we chose to use. Because of material and machine constraints, we were not able to embed our sensor, but needed to simulate the embedding for the most accurate results. A user must also be cautious to protect the fiber within the structure to ensure its longevity and accuracy; however, if the FOS is properly embedded into a material, the strain cause by the curing process of the material as well as the health of the structure can be monitored over time. With this FOS monitoring system, commonly referred to as a nervous system, buildings, bridges and other structures can be properly monitored. In doing so, the structure can be maintained properly to guarantee it operates safely and effectively even after decades of operational and environmental abuse.

2.1.2 Health Monitoring

Health monitoring is often done as a combination or as a supplement to structural monitoring. The goal of health monitoring is to protect a structure or component from failure.

This is done by determining the maximum quantities it can withstand of measurements such as strain and performing maintenance or repairs before those quantities are reached.

Health monitoring is often done in large moving structures such as wind turbines. Wind turbines have been utilized for various processes for centuries. Whether the wind turbine was used for grinding grain or producing electricity the process of capturing the kinetic energy of the wind and converting it to mechanical energy was based on the same idea. Wind turbines face many challenges due to constant rotation and vibration throughout their lifespan. One of the most problematic challenges faced by wind turbines is caused by the stresses and strains that act on the wind turbine blades while rotating. These cyclic stresses occur because of the repetitive rotating motion of the blades which have a direct effect on the materials of the wind turbine. Herbert Sutherland et al preformed an analysis of composite wind turbine blades and provided engineers with essential information regarding fatigue loads and damage predictions (2004). Because of the growing use of wind turbines to produce energy, this project will determine with what resolution a fiber optic sensor can dynamically measure strains on a scaled wind turbine blade. Damage analysis of wind turbine blades requires a description of the fatigue load spectra and the fatigue behavior of blade material. The R-value for a fatigue cycle commonly used when analyzing wind turbine blades is:

$$R = \frac{\sigma_{min}}{\sigma_{max}} \tag{2.1}$$

Where σ_{max} is the maximum stress and σ_{min} is the minimum stress in a fatigue stress cycle (Sutherland & Mandell, 2004). R-values must be considered for reverse loading, tensile values, compression values, and constant values. Goodman diagrams such as in Figure 1, represent cycles-to-failure plotted as a function of mean stress and range along lines of constant R-values (Sutherland 2004).

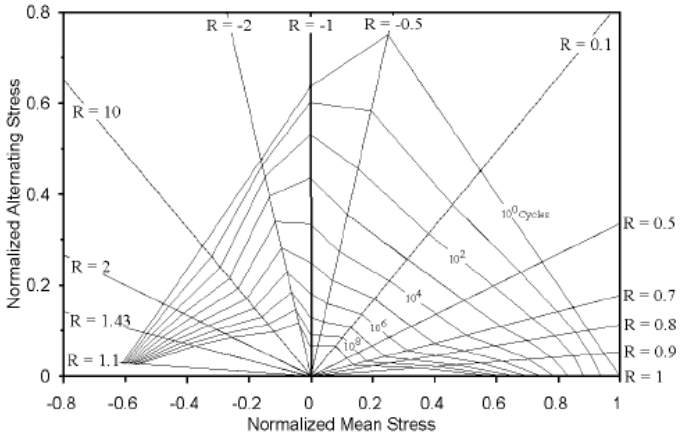

Figure 1 Goodman Diagram of Thirteen R-values for Database Material DD16

The Goodman diagram shows that the alternating stress is at its maximum with an R-value of -1 and a normalized mean stress equal to zero. It is also shows that it is important to consider the various materials that are commonly used in the construction of wind turbine blades because each material reacts differently to stresses and strains. The various materials that make up wind turbines can crack, peel, warp, and disintegrate from the cyclic stresses as well as from all the other forces acting on the structure. In order to prevent wind turbines from malfunctioning due to a lack of preventive measures, researchers and engineers have set out to find a solution that can function in the wind turbines extreme environment. As previously stated, we chose to utilize the electromagnetic and temperature immunity of a fiber optic sensor and apply it to a scaled wind turbine blade because it would survive in these extreme environments with little to no damage.

2.2 Conventional strain sensors

Some of the two most common sensors used to measure strain are the foil strain gauge and the MEMs accelerometer. Both sensors have been used and trusted to measure strain for several

years; however, with advancing technology, the way in which we measure strains also needs to advance.

2.2.1 Foil Strain Gage

The most common type of foil strain gauge consists of a metal foil pattern which is adhered to an insulating flexible backing. The foil gauge measures strain by being attached to an object and as the object deforms the foil is deformed, causing its electrical resistance to change. The resistance chance, usually measured using a Wheatstone bridge, is related to the strain by the quantity known as the gauge factor. Figure 2 shows both a schematic of a conventional foil strain gauge and an internal block diagram of the electrical set up within the gauge. The foil strain gauge is configured in a Wheatstone bridge, with resistors in parallel.

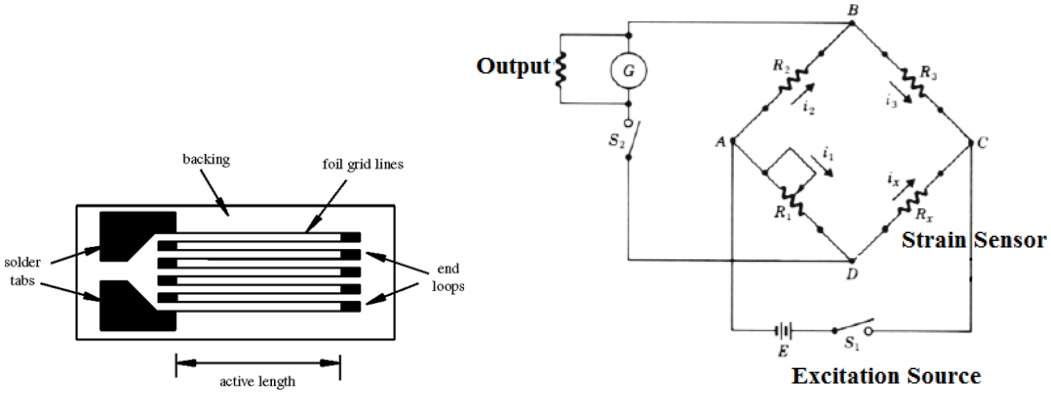

Figure 2 (a) Schematic of Foil Strain Gage (b) Internal Block Diagram of Foil Strain Gage

The resistance seen at the output follows the equation 2.2 and can be simply converted into strain. By exploiting the changes in resistance felt by the gauge at an applied load using equation 2.3.

$$R = \rho \frac{L}{A} \tag{2.2}$$

$$\varepsilon_{xx} = \frac{\Delta R}{FR} \tag{2.3}$$

Where is the resistivity of the material of the gauge, *L* the gage or active length, *R* is resistance and *F* is the gage factor. Values for the gage factor of a conventional foil strain gage are approximately 2.095 (Furlong, 2010).

Though the foil strain gage is inexpensive, simple to use, and suitable in certain applications, it does have several shortcomings. The gage factor of a fiber optic sensor is approximately 25 times the gage factor previously mentioned for the foil strain gage, showing a much higher resolution in the fiber optic sensor. High resolutions are needed in precise applications where measurements of small strains are needed to verify designs and test their performance. The foil strain gage is also not immune to large temperature changes. This causes the foil strain gage to fail or produce unreliable readings in harsh weather conditions or working environments. Another conventional strain sensing device with similar shortcomings is the MEMs accelerometer.

2.2.2 Accelerometer

The MEMs accelerometer, also a common sensor used for strain measurements, is an inertial sensor whose measurements of acceleration can be converted into strain, among other things. Commonly used to measure the dynamic forces acting on an object, an accelerometer is an electromagnetic device that measures acceleration forces an object experiences relative to freefall. Unlike the foil strain sensor, the accelerometer has the capabilities to measure quantities in 1, 2 or 3 directions (Anolog Devices, Inc., 2010). Commonly used low-cost accelerometers are the MEMs ADXL202 and ADXL203. Figure 3 shows both a schematic of a conventional accelerometer and an internal block diagram of the electrical set up within the sensor (Analog Devices, Inc, 2010).

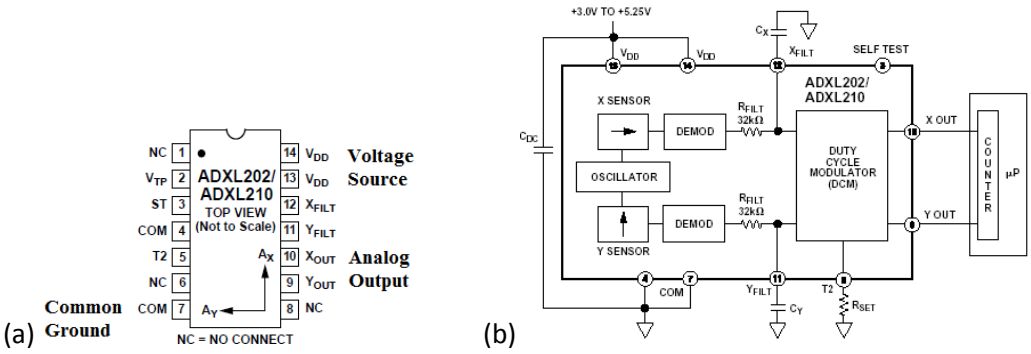

Figure 3 (a) Schematic of MEMs Accelerometer (b) Internal Block Diagram of ADXL202 MEMs Accelerometer

Figure 3 shows one of the many available configurations of MEMs accelerometers, the ADXL202 is a dual axis accelerometer that measures accelerations along the x- and y-axis. The voltage change seen due to dynamic acceleration follows equation 2.4, derived from the position equation.

$$\ddot{y}(t) = -\omega A \sin(\omega t + \phi) \tag{2.4}$$

Where ω is the frequency of excitation, ϕ is the phase shift, t, the time and A the amplitude. By exploiting the amplitude of the sine function, ωA, the strain of the system can be found. The sensitivity of MEMs accelerometers vary depending on application and model, but are slightly higher than that of a foil strain gage. The sensitivity of these sensors is on the order of 300mV/g, with g being the gravitational constant (Analog Devices, Inc., 1999).

Similar to the conventional foil strain gage, the MEMs accelerometer is also relatively inexpensive and easy to use. The MEMs accelerometer provides superior measuring accuracies when compared to the foil strain gage, but the capabilities of a fiber optic strain gauge still surpass the accelerometers. Though the accelerometer can withstand higher temperatures, up to 85 degrees Celsius and requires slightly less power to operate than the foil strain gage, it is still sensitive to electromagnetic interference (Analog Devices, Inc., 1999). This causes the MEMs accelerometer to fail or provide unreliable results when validating design or measuring the

performance of some electronic components or systems, such as an MRI machine used in hospitals or during light strikes on wind turbine blades.

Clearly, higher resolutions and temperature and electromagnetically immune sensors are needed for several applications because of increasing and advancing technologies. We chose to work with fiber optic sensors because none of these problems would cause this kind of sensor to fail, and the resolutions are much higher. Figure 4 summarizes some of the expected and known advantages of using a fiber optic sensor when compared to two conventional techniques.

Characteristics	Foil Strain Gauge	MEMS Accelerometer	Fiber Optic Sensor
Ultra High-Resolution	×	×	✓
Temperature Resistant	×	×	✓
Electromagnetically Immune	×	×	✓
Non-Invasive Design	✓	✓	✓
Commercially Available	✓	✓	✓

Figure 4 Comparison of Strain Sensing Devices

2.3 Optical Fiber Communications

2.3.1 History and development of Optical Fiber Communications

Communications have been critical to human advancement, economic growth, and general prosperity. Not long ago, the only form on information transfer was person to person. Consequently, advancements in civilizations were limited because the rate information travelled was limited. The most recent advancement in communications has been with the use of fiber optic technologies.

To understand the benefits of optical fiber communications, the basics of telecommunications must be explored. In the simplest terms, telecommunications contain a transmitter, channel to

carry the signal, and receiver to move information over long distances. The transmitter is what inputs the information into the channel. Transmissions can be explained by a simple analogy to the vocal cords of the human body. In order to achieve a certain signals, the vocal cords create changes in air pressure in a specific pattern that passes through the air, or channel in which the information propagates. The signal, or changes in air pressure, is then decoded by the air drum, which is analogous to a receiver. In telecommunications, voltage is transferred through a channel in the form of current. Current is output at the receiver is seen as a changing voltage, much like the sensing devices described in section 2.2.

The media at which the information travels limits its accuracy and speed. Copper and other metals have been typically used because of its high conductivity and inexpensive price. Different materials obviously have different material properties which determine the bandwidth, or capacity, of information that can be transferred at any one time. Information is coded in different frequencies travelling through the channel whose summation can be found through Fourier synthesis. As signal distances increases over 300 meters, copper wires become uneconomical and unreliable as a means of information transmission because of a weakening signal.

Different materials have been used to improve the disadvantages of copper for information transfer, one of which is the coaxial cable. A coaxial cable still contains a central conducting wire typically made of metal, surrounding by an insulation material, and an outer conducting material. The electromagnetic waves are carried through the insulator of the cable rather than the core or outer cable. Consequently, higher frequencies could be used, which increases the bandwidth, over longer distances without major attenuation.

Coaxial cables seemed to solve many of the initial problems with bandwidth and long-distance information travel until the inventions of high bandwidth media, including televisions and the internet. These cables also may provide unreliable information transfer if used in the previously mentioned structural and health monitoring situations as they are not immune to electromagnetic interference. Radio waves are more commonly used today for information transfer, as their electromagnetic waves can be carried over much longer distances with greater accuracy; however, radio waves are also susceptible to interference. Each systems disadvantage has been more or less solved by the invention and design of optical fiber. Optical fiber allowed for significantly more bandwidth and do not contain metal limiting special and electrical loss of information.

2.4 Principles of Operation – Fiber Optics

2.4.1 Design of Fiber Optics

The design of optical fibers is critical to their function. An optical fiber is made from a glass core and cladding, commonly made from the material silica. Figure 5 shows a simplified cross section of a fiber optic cable (Qwick Connect, 1999). The buffer, strength material and jacket are option with the core and cladding being the key to fiber optic technology. Fiber optics can be made of multimode or singlemode fiber, with the main difference between the two the size and propagation of light. Multimode fiber typically had a core and cladding diameter of 50 micrometers and 125 micrometers, respectively. A singlemode fiber typically has a smaller core and cladding diameter of 8 micrometers and 62.5 micrometers, respectively.

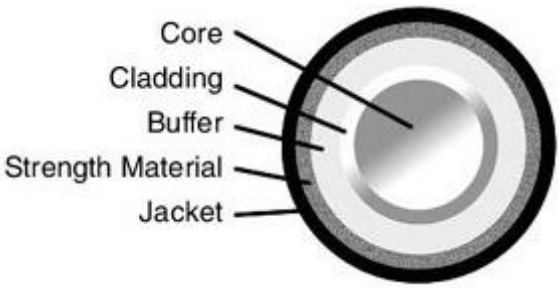

Figure 5 Fiber Optic Cable Cross Section

2.4.2 Physics of Fiber Optics

As previously mentioned, light propagation through a fiber is determined by the type of fiber. In single mode fiber, light travels along one optical axis, where in a multimode fiber, light travels in a much more complex manner. Figure 6 shows a simplified pattern of light propagation through single and multimode fibers.

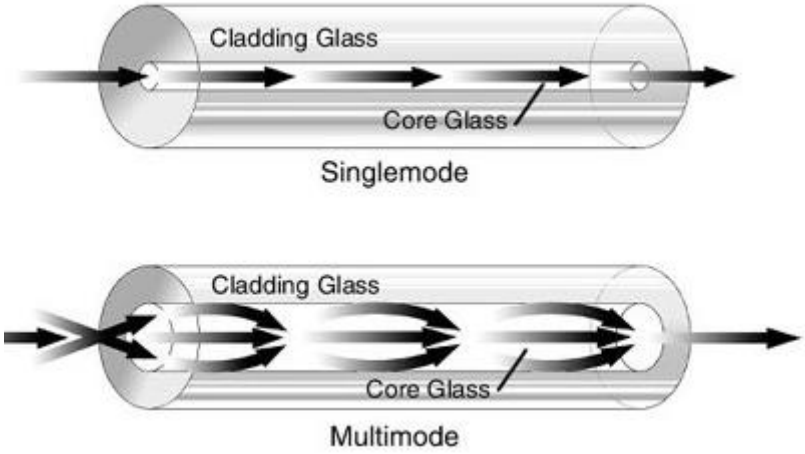

Figure 6 Light Propagation through Singlemode and Multimode Fiber

Though the exact mathematics behind light propagation through the two main types of fiber is complex, the physics behind the light travel is governed by one equation. Light propagation through a fiber core is due to total internal reflection, as shown in Figure 7.

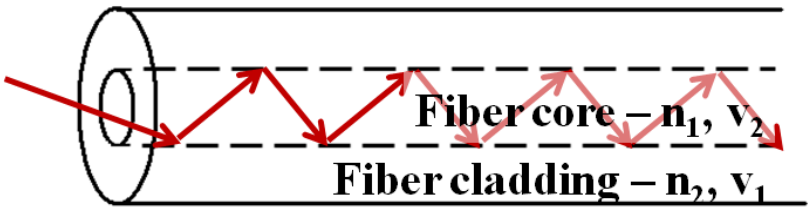

Figure 7 Total Internal Reflection

Each fiber has a fiber core with an index of refraction higher than that of the fiber cladding. It is because of this, light does not escape through the fiber walls. This phenomenon is governed by equation 2.5, Snell's law:

$$\frac{\sin(\theta_1)}{\sin(\theta_1)} = \frac{v_1}{v_2} = \frac{n_2}{n_1} \tag{2.5}$$

With θ the angle at which light enters the fiber, v the velocity of light travel in each media and n the index of refraction of each media. The condition of total internal reflection is satisfied if n_1 is greater than n_2, as is true in all optical fibers (Yin, Yu, & Ruffin, 2008).

2.5 Fiber Optic Sensor (FOS) Configurations

Several fiber optic sensor configurations exist for a variety of applications including strain, pressure and temperature sensing, among others. We chose to focus on two fiber-optic strain sensors whose mechanical and optical properties change with an applied force – the Fiber Bragg Grating and the Fabry-Perot Interferometer.

2.5.1 Fiber Bragg Grating

This Fiber Bragg Grating sensor has become increasingly popular for strain and temperature measurement ever since it's creation in 1989. This interest in FBGs is the result of its ability to directly correlate the wavelength of light and the change in the desired strain. FBGs are structures made in core of the single mode optical fiber characterized by periodic changes in

the value of the refraction index occurring along the axis of the optical fiber. Because of these changes, part of the optical wave transmitted by the optical fiber is reflected by the Bragg's grating structure, and the remainder is propagated along the optical fiber's core without any loss (FBGS Technologies, 2009).

If the fiber is strained from applied loads then these gratings will change accordingly and allow a different wavelength to be reflected back from the fiber. The strain experienced by the FBG sensor can calculated by Equation 2.6 where $\Delta\lambda$ is the wavelength reflected and λ is the original wavelength.

$$\varepsilon = \Delta\lambda/\lambda \quad (2.6)$$

Calibrating the sensing equipment to read the changes in reflective index makes it possible to monitor temperature and strains by only analyzing the specific wavelength of the light source being reflected.

2.5.2 Fabry-Perot Interferometer (FPI)

The first Fabry-Perot interferometer was a "bulk-optics-version" invented in the nineteenth century. This invention allowed for high-resolution spectroscopy (Yin, Yu, & Ruffin). Fiber optic versions of this Fabry-Perot have been created based on several principles and equations discovered and studied from this bulk version. The first of these fiber optic Fabry-Perot interferometers (FFPI) was created in the 1980s and were commonly used for sensing temperature, strain and ultra-sonic pressure (Yin, Yu, & Ruffin, 2008). Since then, changes in materials used and structure of the FFPI has been adapted for higher resolutions and different applications, but the principles are still the same.

Fabry-Perots can be made to be fixed, know as an etalon, or mechanically movable. Measurements from etalons are from changes in angle or index of refraction as light travels

through the fixed cavity while mechanically movable FPIs measure changes in the cavity length (Measures, 2001). The configuration of an FPI consists of two parallel, semi to highly reflective mirrors or coated fiber tips spaced a distance apart. The distance between the two fiber tips is generally on the order of nanometers and, depending on the gauge length (the active sensing region, defined as the distance between fusion welds) ranges of mechanical or thermal strain the sensor has designed to measure (Belleville & Duplain, 1993). The sensor used in this project has been made to be nearly immune to the effects of thermal strain. Mechanical strains can be measured applying the basic definition of strain to this sensor, as follows:

$$\varepsilon = \frac{\Delta d}{d_o} = \frac{(\delta_{cavity})}{L_{gauge}} \tag{2.7}$$

Where δ_{cavity} is the change in the cavity length from a given load. This can be measured in a change in optical phase of the output light intensity. For the FPI sensor used in this project, L_{gauge} is approximately 5 millimeters and δ_{cavity} ranges between 8,000 and 23,000 nanometers, depending on the applied strain.

2.6 Principles of Operation – Fabry- Perot Interferometer (FPI)

2.6.1 Common Fabry-Perot Configurations

In this project, we chose to utilize the Fabry-Perot Interferometer. The Fabry-Perot has three common configurations, shown in Figure 8. Each of the three configurations still contain a cavity surrounded by two semi-reflective tips allowing light to propagate and reflect back in a similar manner for each.

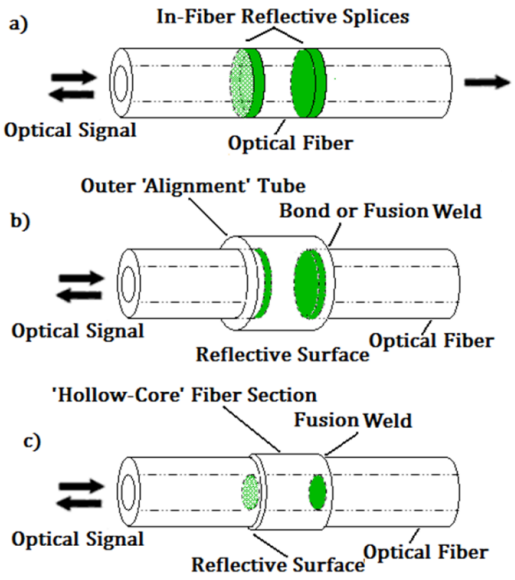

Figure 8 Common Fabry-Perot Configurations

The intrinsic Fabry-Perot interferometer (IFPI), shown in Figure 8a, is fully contained within the fiber, with no micro-capillary surrounding the distance between reflective mirrors. The IFPI is made by creating one or two reflective fusion splices within the fiber (Measures, 2001). The medium between reflective surfaces is no longer air, but optical fiber. To build an IFPI, a solid length of optical fiber is taken and two in-fiber reflective splices are created to form the sensors cavity.

The extrinsic Fabry-Perot (EFPI), shown in Figure 8b, is the most commonly used FPI in strain-sensing applications because it is easier to manufacture than the intrinsic FPI (IFPI), it has a protective capillary tube which also acts as an alignment mechanism, and allows for no transverse coupling (Measures, 2001). When studying the benefits of no transverse coupling in 1991, Sirkis and Haslach showed the extrinsic version of this sensor could "evaluate more directly the axial component of strain in the host material" (Measures, 2001). To build an EFPI, a cavity is created between two fiber ends which act as the two reflective surfaces by being coated in a semi-reflective to reflective material. These fibers, which can be singlemode or multimode,

are inserted into the capillary tube and fused into place. Another advantage of the EFPI sensor is the gauge length (distance between the fused welds) is generally greater than the cavity length, allowing the use of lasers with larger coherence lengths; however, extreme care must be used to determine this gauge length, if it is not previously known (Measures, 2001).

The third common type of FPI is the in-line fiber etalon (ILFE), as shown in Figure 8c. As previously mentioned, etalons have fixed reflective surfaces. The ILFE is created by welding a hollow-core fiber to the cleaved ends of two optical fibers with reflective coatings. Unlike both the extrinsic and intrinsic FPIs, the ILFE does not have any physical discontinuities after the welding (Measures, 2001). Though all three common types of FPIs sense using the basic principles of interference, the ILFE does not measure strains by change in cavity length. Strains are measured by differences in index of refraction and angle changes (Yin, Yu, & Ruffin, 2008).

2.6.2 Light Propagation and Governing Equations – Fabry-Perot Interferometer

The first intrinsic FFPI was created by Lee and Taylor in 1988 coating fiber ends with TiO_2 to create two internal mirrors (Measures, 2001). Later, fiber tips were coated with multi-layer TiO_2/SiO_2 films to create the semi-reflective "mirrors" both intrinsic and extrinsic FPIs contain (Measures, 2001). This technique is the most widely used for coating fiber tips of FFPIs, but the material used to create the film varies. Light propagation through the cavity can be seen in Figure 9.

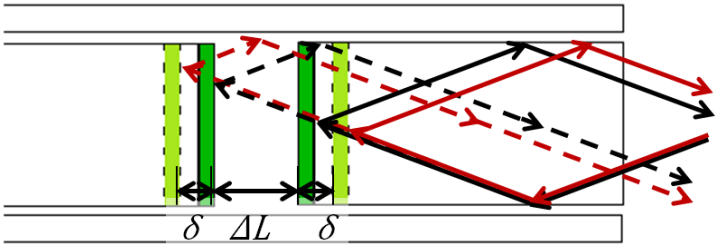

Figure 9 Light Propagation through FPI Cavity

Light propagates through the cavity containing semi-reflective mirrors. Some of the light is transmitted and some is reflected. The returning light interferes resulting in black and white bands known as fringes caused by destructive and constructive interference. The intensity of these fringes vary due to a change in the optical path length related to a change in cavity length when uniaxial force is applied. This phenomenon can be quantified through the summation of two waves. By multiplying the complex conjugate (equation 2.8) and applying Euler's Identity (equation 2.10) we obtain the following equation of reflected intensity at a given power for planar wave fronts (equation 2.11) (Gangopadhyay, 2004):

$$I = (U_1 + U_2)(U_1 + U_2)^* \tag{2.8}$$

$$I = A_1^2 + A_2^2 + A_1A_2e^{(\phi_1-\phi_{2)i}} + A_1A_2e^{(\phi_2-\phi_{1)i}} \tag{2.9}$$

$$e^{\phi i} = cos\phi + isin\phi \tag{2.10}$$

$$I = A_1^2 + A_2^2 + 2A_1A_2\cos(\Delta\phi - \Delta\theta) \tag{2.11}$$

With A_1 and A_2 representing the amplitude coefficients of the reflected signals due to the reflectivities, R_1 and R_2, respectively. The above equation can be changed to represent only intensities by substituting $A_i^2=I_i$, i=1,2:

$$I_R = I_1 + I_2 + 2\sqrt{I_1I_2}\cos(\Delta\phi_1) \tag{2.12}$$

Where I_1+I_2 will remain constant, due to the power input of the system and the coefficient of the cosine function will determine the contrast of fringes. The argument of the cosine function is related to the initial cavity length, ΔL and change in cavity length δ with $\Delta\phi$ and $\Delta\theta$ defined as follows

$$\Delta\phi = \frac{2\pi}{\lambda}\Delta L \tag{2.13}$$

$$\Delta\theta = \frac{2\pi}{\lambda}2\delta \tag{2.14}$$

The change in round trip phase lag, as defined in equation 2.14, is directly correlated to the pattern of fringes (Gangopadhyay, 2004). From these equations we were able to predict the fringe patterns produced by different amounts of stress, as shown in Figure 10 (Vest, 1979).

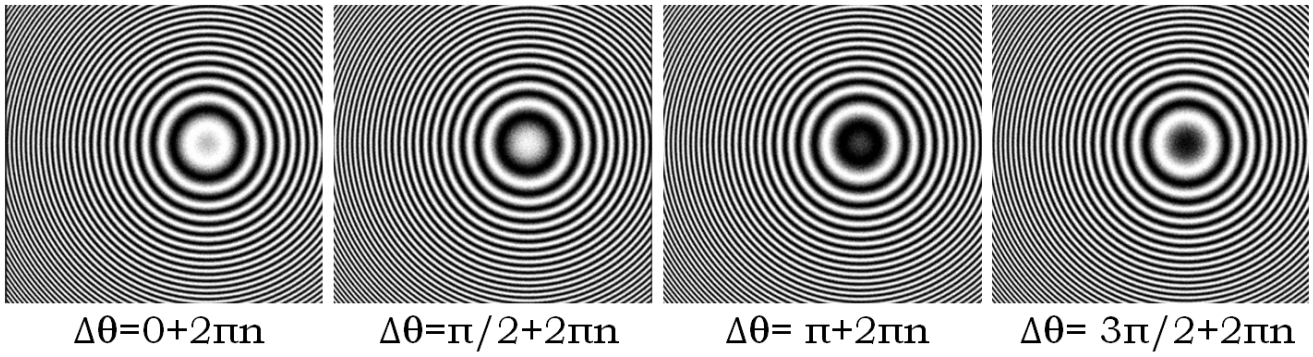

Figure 10 Theoretical Fringe Predictions for Different Applied Strains

The intensity of the fringes follow a periodic function as force is applied, as shown in Figure 11. By exploitation of interference characteristics, we can measure strains.

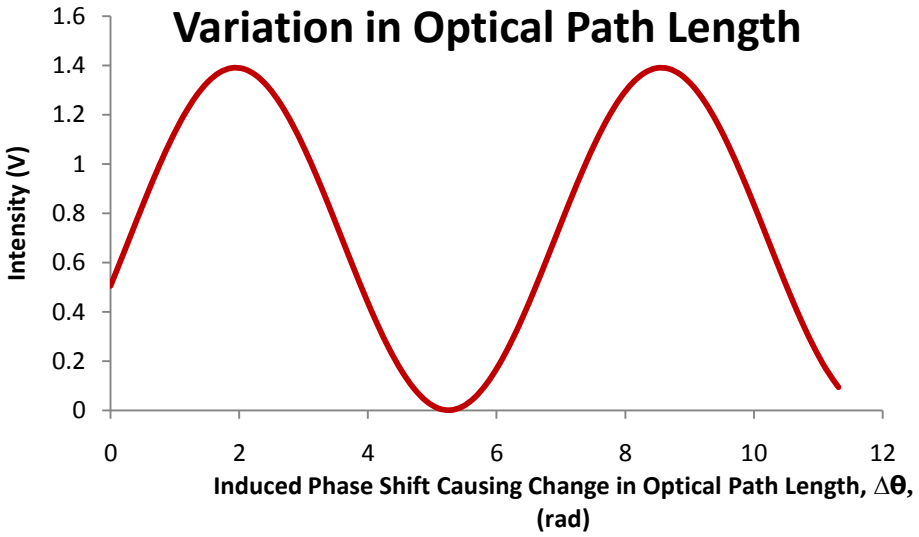

Figure 11 Intensities Produced from Phase Shifts Induced by Applied Strains

2.7 Development of Miniaturized Fabry-Perot Interferometer

After analyzing the principles of operation of a bulk Fabry-Perot Interferometer, a manufactured miniaturized Fiber Fabry-Perot Interferometer strain sensor needed to be explored. A sensor was needed that could be customized to an application where sensor design and environmental operation conditions are crucial for proper implementation of the sensor.

There are not many manufacturers that produce miniaturized FPI strain sensors and as a result FISO Technologies Inc. was chosen for this project. FISO Technologies, located out of Canada, is a leading developer and manufacturer of fiber optic sensors. FISO Technologies Inc.'s FOS-N strain sensor was chosen for its high sensitivity and resolution, resistance to temperature, no interference due to cable bending, non-invasive design, as well as its immunity to electromagnetic interference. The final specifications of the fiber FPI strain sensor that was purchased for this project are: functional with 830nm light source, 1m long multimode fiber with an ST connector, core diameter of 50µm, cladding diameter of 125µm, 1mm outer diameter PTFE coating, operating temperature of -40°C to 250°C, 20mm bare tip, and has a sensing range of +/- 1000µm.

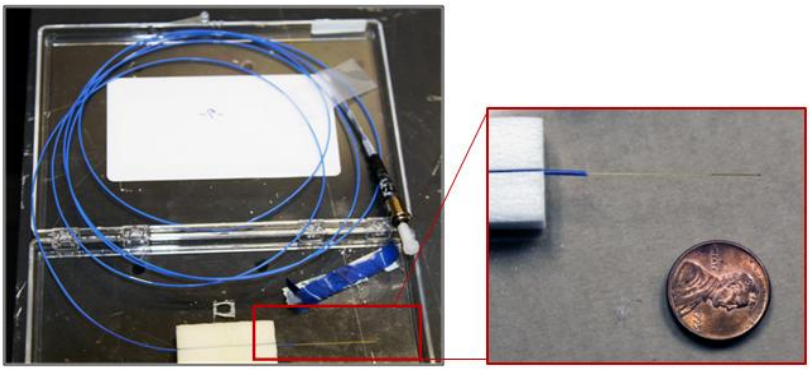

Figure 12 FISO Technologies Inc. fiber FPI strain sensor

Figure 12 shows how the FISO Technologies FPI strain sensor is packaged after it is manufactured. The main component of the FPI's design is the glass capillary at the end of the

multimode fiber, which contains the sensing cavity. This glass capillary is seen in a magnified view with all of its dimensions in Figure 13.

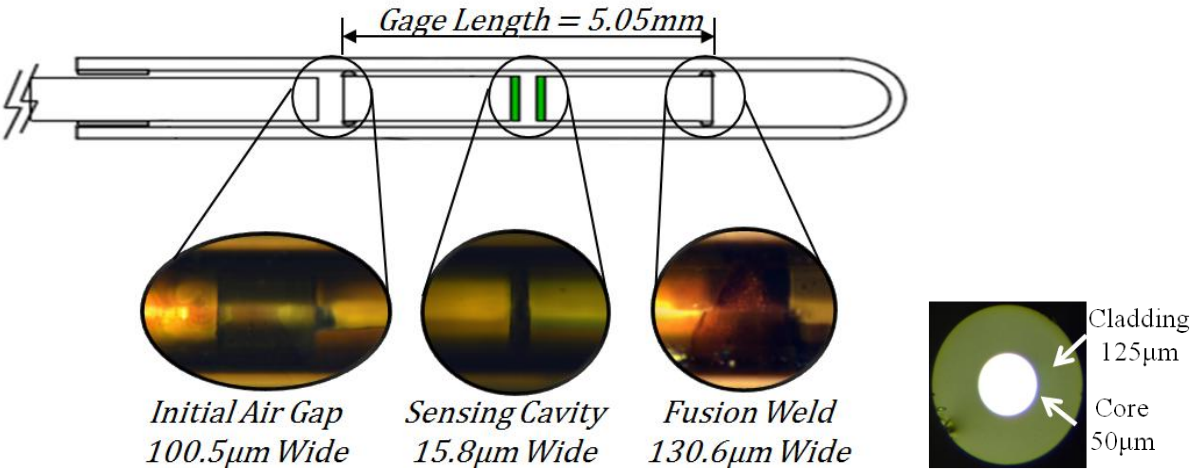

Figure 13 Magnified fiber FPI strain sensor

Within the capillary, there are three fusion welds which attach the three fibers to the glass capillary wall. The main component of the FPI is the sensing cavity, seen by the highlighted green faces in the middle of the capillary, has a width of 15.8µm and this width was measured using a high-resolution microscope. Once we purchased a miniaturized fiber Fabry-Perot Interferometer strain sensor we set out on validating its functionality with the help of analytical and computational finite element analysis calculations.

3 Methods

3.1 Verification of Sensor Displacement Linearity

Analyzing the deformation behavior of the sensor, the glass capillary and its components, as a load is applied was important to the project as a whole. The sensor's linearity must be verified using finite element analysis because if it is not linear then the future experiments and other calculations will not work because they are based on a linear sensor.

Finite Element Analysis (FEA) is a numerical technique for obtaining approximate solution to a wide variety of complex engineering problems. The variables of the problems are related by a series of differential and integral equations. FEA is commonly used in the aeronautical, biomedical, and automotive industries in research and development of their products. FEA is not limited to structural analysis though, it can also help analyze thermo, electromagnetic, and fluid environments. FEA uses a complex system of points called nodes, which make a grid called a mesh, as seen in Figure 15, in a proceeding section. This mesh is programmed to contain the material and structural properties that define how the structure will react to certain loading conditions (Widas, 1997). FEA can be performed both analytically by hand and computationally with the help of FEA software such as ANSYS.

In the case of using ANSYS, a computer is used to perform the calculations needed to find solutions to the differential and integral equations, producing results to graphically show how the structure behaves. Sometimes the computer based FEA provides more opportunities for faster and more accurate results when analyzing a structure than analytical calculations. However, both analytical and computational finite element analysis techniques are extremely useful when observing the behavior of a structure such as our FPI strain sensor.

3.1.1 Analytical Modeling to Prove Linearity

The first approach is based on a finite element analysis spring equivalent model that has five elements, six nodes, a fixed restraint at the flat end of the sensor, and an axially applied force in the x-direction. Figure 14 shows the spring equivalent model used in the analytical calculations.

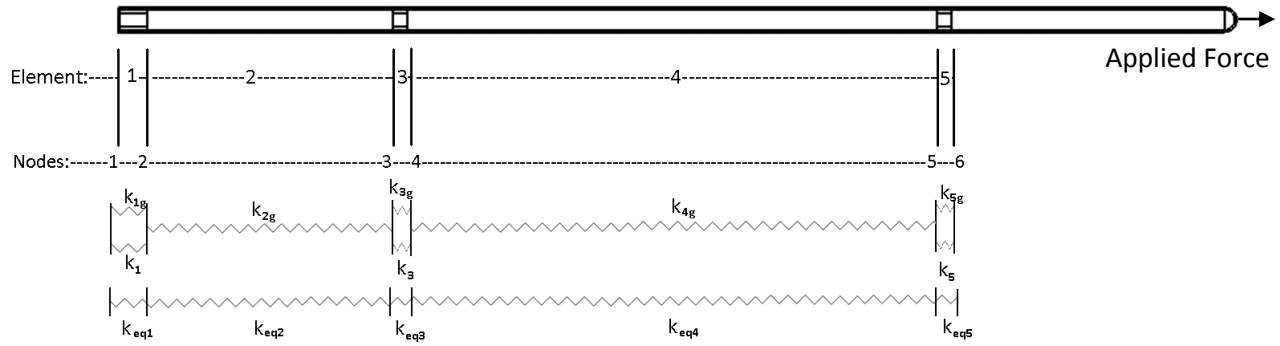

Figure 14 Analytical Spring Equivalent Model of FPI Sensor

It is important to note that the glass capillary and the three fusions welds are what make up the basis for the spring equivalent model. The three pieces of fiber are not included in the model because they do not come in direct contact with the capillary wall. Instead, the fusion welds are in direct contact with the capillary wall and thus are the components of the sensor that experience the deformations due to an applied force. As the welds deform, the fiber pieces within the sensor move which in turn alters the width of the sensing cavity and the strain measurements.

Once the spring equivalent model was made the spring equivalent constants for each of the five elements could be formed. The spring equivalent constant, seen in Equation 3.1, is equal to the cross sectional area of the material multiplied by the elastic modulus of the material and then divided by the length of the element.

$$k = \frac{AE}{L} \tag{3.1}$$

From Equation 3.1 we began to solve for the equivalent spring stiffness of the global system. This was done by calculation the spring equivalent constant, Equation 3.1, for the glass capillary and fusion weld of each element. Equation 3.2a through 3.2e shows that once the spring constants were calculated for each of the components of the elements the equivalent spring constants for the individual spring constants of the elements in parallel could be calculated.

Element 1: $k_{eq\,1} = k_1 + k_{1g}$ (3.2a)

Element 2: $k_{eq\,2} = k_{2g}$ (3.2b)

Element 3: $k_{eq\,3} = k_3 + k_{3g}$ (3.2c)

Element 4: $k_{eq\,4} = k_{4g}$ (3.2d)

Element 5: $k_{eq\,5} = k_5 + k_{5g}$ (3.2e)

Once the equivalent spring constants for the parallel components have been developed the equivalent spring constant for the elements in series can be formed in Equation 3.3. This is the last step before calculating the total displacement of the sensor as a whole.

$$k_{eq,total} = \frac{1}{\left[\left(\frac{1}{k_{eq\,1}}\right)+\left(\frac{1}{k_{eq\,2}}\right)+\left(\frac{1}{k_{eq\,3}}\right)+\left(\frac{1}{k_{eq\,4}}\right)+\left(\frac{1}{k_{eq\,5}}\right)\right]} \quad (3.3)$$

From Equation 3.3 the global displacement of the sensor, Equation 3.4, was calculated and an applied force of 4mN was used in this calculation. The 4mN force was chosen so that the calculations would remain within the value of a one fringe.

$$Global\ Displacement: u = \left(\frac{P}{k_{eq,total}}\right) \quad (3.4)$$

After solving for the global displacement of the sensor, the displacements at the six nodes are to be solved for using the matrix equation for linear springs of each element, Equation 3.5.

Element n: $\begin{bmatrix} k_{eq,n} & -k_{eq,n} \\ -k_{eq,n} & k_{eq,n} \end{bmatrix} * \begin{pmatrix} u_n \\ u_{n+1} \end{pmatrix} = \begin{pmatrix} f^n_{node} \\ f^n_{node} \end{pmatrix}$ (3.5)

Where $f_{node}^{n} = force\ of\ element\ 'n'\ closest\ to\ a\ particular\ 'node'$

The matrix equations for linear springs of each element are utilized to form the global stiffness matrix, Equation 3.6, and from here the nodal force equations can be developed, Equations 3.7a to 7f.

$$\begin{pmatrix} k_{eq1} & -k_{eq1} & 0 & 0 & 0 & 0 \\ -k_{eq1} & (k_{eq1}+k_{eq2}) & -k_{eq2} & 0 & 0 & 0 \\ 0 & -k_{eq2} & (k_{eq2}+k_{eq3}) & -k_{eq3} & 0 & 0 \\ 0 & 0 & -k_{eq3} & (k_{eq3}+k_{eq4}) & -k_4 & 0 \\ 0 & 0 & 0 & -k_4 & (k_{eq4}+k_{eq5}) & -k_5 \\ 0 & 0 & 0 & 0 & -k_5 & k_5 \end{pmatrix} * \begin{pmatrix} u_1 \\ u_2 \\ u_3 \\ u_4 \\ u_5 \\ u_6 \end{pmatrix} = \begin{pmatrix} F_1 \\ F_2 \\ F_3 \\ F_4 \\ F_5 \\ P \end{pmatrix} \quad (3.6)$$

$$F_1 = (k_{eq1} * u_1) \quad (3.7a)$$
$$F_2 = (k_{eq1} + k_{eq2}) * u_1 - (k_{eq2} * u_3) \quad (3.7b)$$
$$F_3 = (-k_{eq2} * u_2) + (k_{eq2} + k_{eq3}) * u_3 - (k_{eq3} * u_4) \quad (3.7c)$$
$$F_4 = (-k_{eq3} * u_3) + (k_{eq3} + k_{eq4}) * u_4 - (k_{eq4} * u_5) \quad (3.7d)$$
$$F_5 = (-k_{eq4} * u_4) + (k_{eq4} + k_{eq5}) * u_{35} - (k_{eq5} * u_6) \quad (3.7e)$$
$$P = (-k_{eq5} * u_5) + (k_{eq5} * u_6) \quad (3.7f)$$

With Equations 3.7a to 3.7f, mathematic software called MathCAD was used to solve for the nodal displacements of the sensor. The complete calculations performed in the analytical calculations can be seen in Appendix A.

3.1.2 Computational Modeling to Prove Linearity

The analytical calculations are based on the force and displacement of the sensor; however, we are also interested in studying the stresses at the welds to see if their deformations will affect the linearity of the sensing cavity.

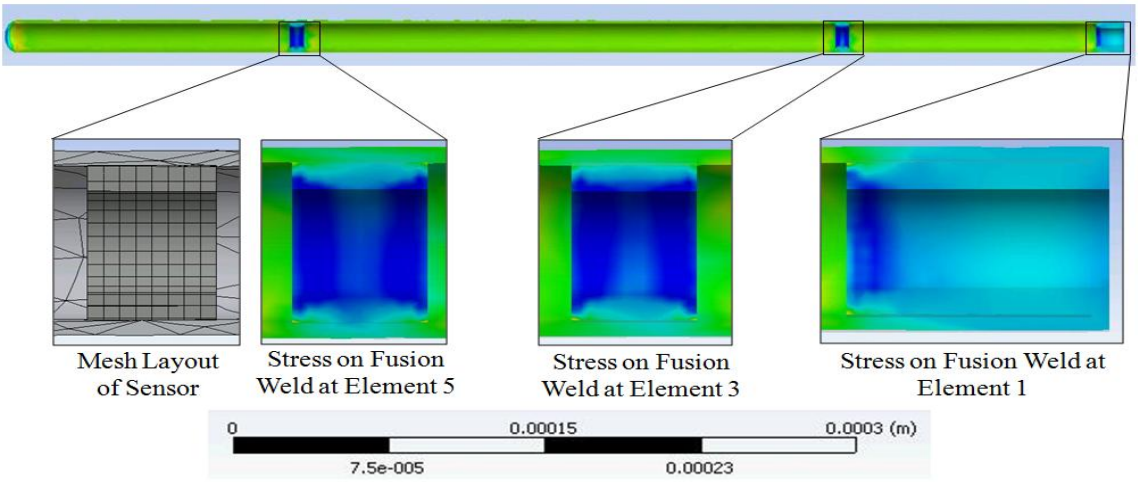

Figure 15 ANSYS Computational Model of FPI Strain Sensor

A finite element analysis software, ANSYS Workbench, was utilized to develop a fully three-dimensional model of our FPI strain sensor. This was used to verify the analytical displacement results as well as measure the strains experienced by the sensor. A computer aided design program, SolidWorks, was used to make the initial fully three dimensional model of the sensor. This model was then imported into ANSYS Workbench with the correct constraints, applied force, and material properties just as in the analytical model as seen in Figure 15. The ANSYS contained a great deal more elements and nodes than the analytical model with 8076 elements and 22183 nodes. After the complex model was tested and the results were analyzed, comparisons between the analytical and computational calculations were made.

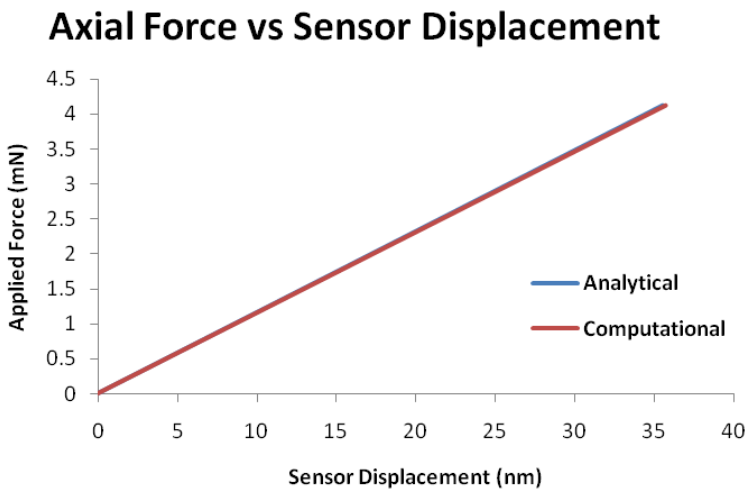

Figure 16 Analytical and Computational Agreement of Linearity of FPI Sensor

As Figure 16 displays, there is a nearly perfect agreement between the analytical and computational calculations with less than 1% error between them. Since the FPI sensor's linearity was verified using two different finite element methods, we now had to set out on designing an opto-mechanical setup for use of our FPI sensor.

3.2 Realization Opto-Mechanical Setup for use of FPI Sensor

It was determined from our background research that our fiber FPI strain sensor typically utilized white light when operating. Therefore, a light source is needed that is compatible with both the FPI sensor as well as with a detector.

The opto-mechanical setup begins with a pigtailed laser diode (*PLD*) which emits light in the 830nm rand of the infrared line with a power of 1mW. This diode is controlled by a laser diode controller (*LDC*) which has a PID built in which helps stabilize the temperature and current of the diode when attached to laser cooler. The output of the pigtailed laser that exits the FC connector (*FC*) at the end of the sensor's fiber is connected to a Z-axis translator *(* ZT). This Z-axis translator helps focus the divergent light onto a 20X objective lens mounted to an X-

Y-axis translator (*20XYT*). This collimated light is sent into a 50:50 beam splitter cube (BS) where fifty percent of the light is split towards the FPI sensor (*FPI*) and the other fifty percent is not used.

The light that is sent to the sensor is focused onto the 50µm core of the sensor's multimode fiber. This focusing is accomplished with the help of another 20X objective lens mounted to an X-Y-axis translator which focuses the light onto the fiber core which is able to adjust via a Z-axis translator which has the FPI fiber's ST connector (*ST*) attached to it. The light travels through the fiber and into the sensing cavity and then back reflects out the same optical axis it came in. This back reflected light passes through the 20X objective lens and is collimated into the beam splitter and once through the beam splitter the light is sent into the photodetector (*PD*). The photodetector's output is digitized by a 16-bit data acquisition system (*DAQ*) and a processing computer (*PC*) is used to calculated the strain values.

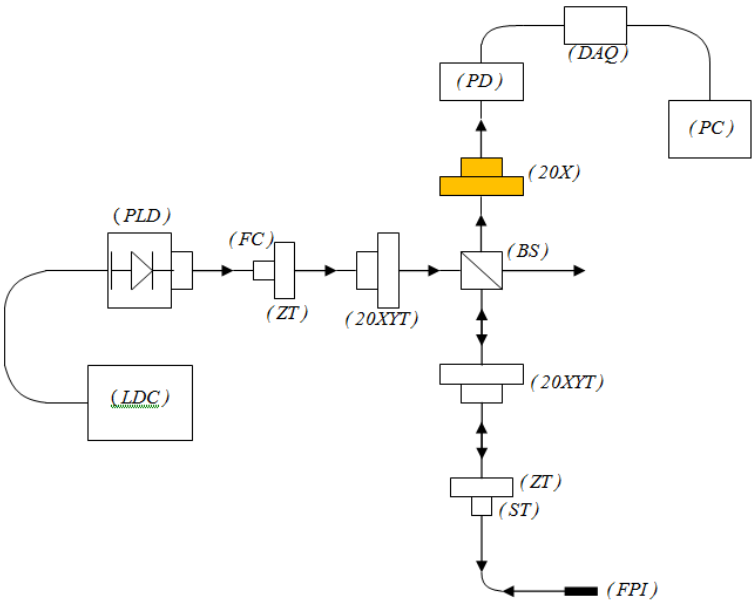

Figure 17 Final Opto-Mechanical Design

It is important to take note that the highlighted 20X objective lens in Figure 17 was added later on in our project. The rest of the opto-mechanical setup is the remained the same as the

prior setup, the only addition was the third 20X objective lens. The lens was added because there was a large amount of noise being recorded in our data and we were having trouble analyzing it properly in order to calibrate our complete setup. As a result, an additional 20X objective lens was added so that the light could be directly focused into the photodetector's sensing region in order to successfully reduce the noise in the recordings. Refer to Appendix B for complete descriptions of all the components used in our projects experiment.

3.2.1 Vibrometer Design

After we finalized our opto-mechanical setup design, our fiber FPI strain sensor could be evaluated in our experiments. In addition to the final opto-mechanical setup, we required the use of addition equipment for our dynamic experiments. Our cantilever beam and turbine blade model with FPI sensor attached, were vibrated using a Jordon EV-30 piezoelectric shaker. To control the frequency of the piezoelectric shaker a Pragmatic 2414A waveform generator and a ThorLabs MDT694A piezo controller were used. The displacement of the vibrating cantilever beam and turbine blade was measured using a Polytec OFV fiber vibrometer which utilizes a reference beam as well as a probe beam to complete the measurements. The vibrometer measurements are then digitized by a DAQ system so that a computer can process the final dynamic test calculations.

3.2.2 Holographic Time Averaged Design

We utilized a previously constructed holography setup that is in the CHSLT lab to perform our holographic time averaged tests. This holographic setup allowed us to view the bending modes of our cantilever beam and turbine blade.

3.3 Calibration of the System

Once the Fabry-Perot Interferometer was incorporated into our opto-mechanical setup, the system needed to be calibrated. Calibration was done by attaching the FPI to a cantilever beam based on analytical and computational calculations of the areas of maximum strain when a static load has been to the free end of the beam. The maximum applied weight was determined to stay within one fringe variation.

3.3.1 Analytical Modeling

The cantilever beam can be modeled by a free body diagram. Figure 18 shows the cantilever beam with the fixed end, left, and free end, right. Figure 18 also shows the free body diagram of the corresponding cantilever beam. The reaction forces at the wall are represented by forces in the horizontal and vertical directions, R_x and $R_{y,}$ respectively. Based on the right hand rule, the bending moment of the beam is counterclockwise and represented using the variable M. At the free end of the beam of length, L, is an applied force, F.

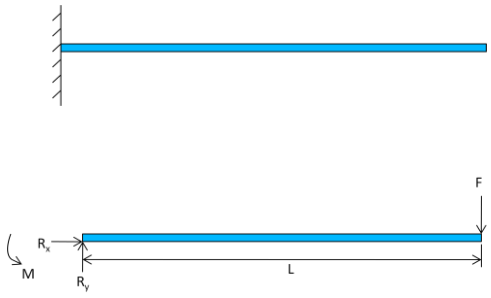

Figure 18 Free Body Diagram of Cantilever

The strain on the beam can be calculated in terms of the applied force, shown in equation 3.8 and 3.9, where F is the applied force, L is the length of the beam, c is the distance from the

center of the beam along the *y-direction*, *b* is the width of the base, *t* is the thickness, and *E* is young's modulus.

$$\varepsilon_{xx} = \frac{Mc}{I_{zz}E} \tag{3.8}$$

$$\varepsilon_{xx}(F) = \frac{12FLc}{bt^3E} \tag{3.9}$$

Appendix C shows the step by step calculation for the strain-force relationship that has been summarized above. This relationship can be graphed to show that strain and applied force on the cantilever beam have a linear relationship, Figure 19.

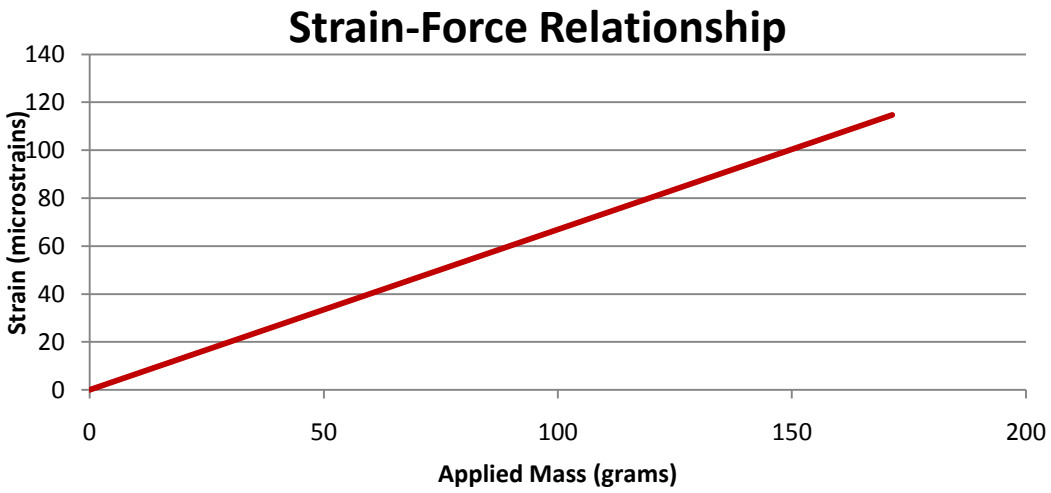

Figure 19 Strain-Force Relationship

In addition to identifying the force strain relationship, it is critical to determine the area of maximum strain when a load is applied to the end of the cantilever beam. As a result, further analysis must be done on the cantilever by taking a "cut" through the beam. The free body diagram is now shown below, where *V* is equal to the shear force on the cross section al area of the cut and *N* is the force normal the cross sectional area.

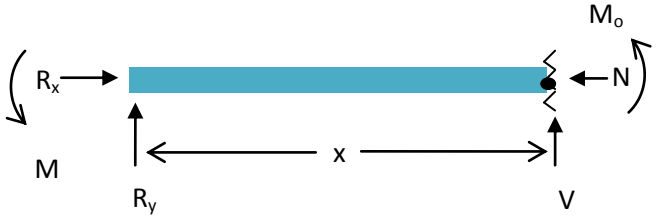

Based on the diagram, the summation of the moments about the cut in the beam, M_o, is quantified by equation 3.10:

$$M_o = R_y(x) - FL \tag{3.10}$$

Equation 3.9 can be used to plot the relationship between the strain response as a function of varying the applied force and at different locations (x) from the fixed end of the beam. A three dimensional color plot of the results are shown below in Figure 20. Clearly, the maximum strain occurs when x is equal to zero, corresponding to the point where the beam is fixed to the wall. The strain also increases as the applied force increases, as expected. Therefore, analytical calculations show that statically loading the cantilever with increasing weight will results in higher strains at the fixed end of the beam.

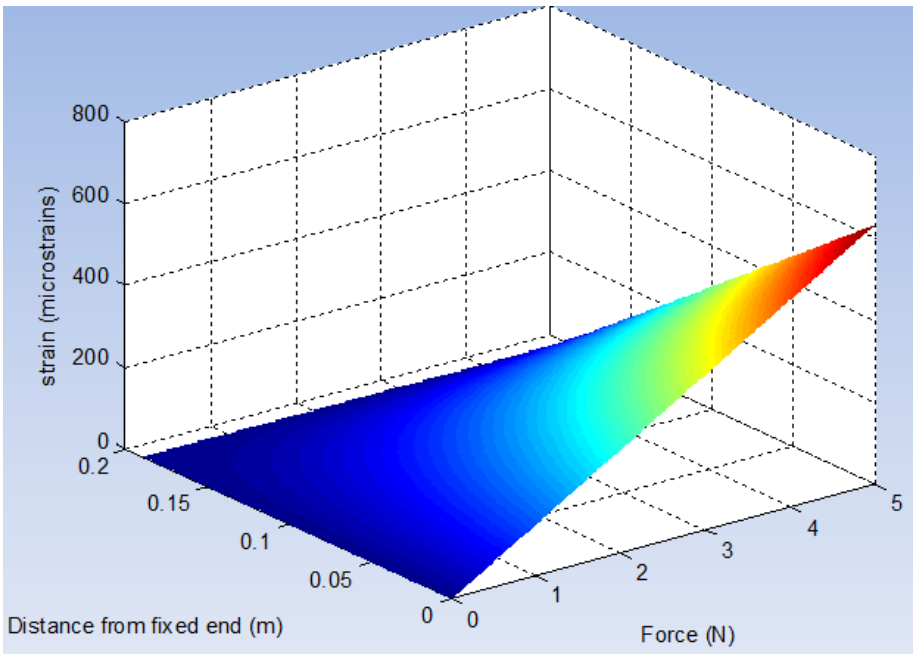

Figure 20 Strain-Force-Location Relationship

In order to calibrate the FPI, the relationship between the intensity of light at the output of the strain must be derived. The general equation for intensity was outlined in the background

and is shown in below in equation 3.11. $\Delta\Phi$,is defined as the change in phase and is equal to the wave number, $\frac{2\pi}{\lambda}$, multiplied by the length of the sensing cavity region and the strain in the *x-direction*, equation 3.12. This value for the change in phase was substituted into intensity equation and it is now possible to predict the output intensity of light as a function of the induced strain, equation 3.14. In addition, this relationship is plotted in Figure 21, where the intensity ranges from zero to $2I_o$.

$$I = 2I_o[1 + \cos(\Delta\phi)] \tag{3.12}$$

$$\Delta\phi = \frac{2\pi(\varepsilon_{xx} L_{cavity})}{\lambda} \tag{3.13}$$

$$I = 2I_o\left[1 + \cos\left(\frac{2\pi(\varepsilon_{xx} L_{cavity})}{\lambda}\right)\right] \tag{3.14}$$

From equation 3.14, we can determine the theoretical strain at any given voltage, as seen in Figure 21.

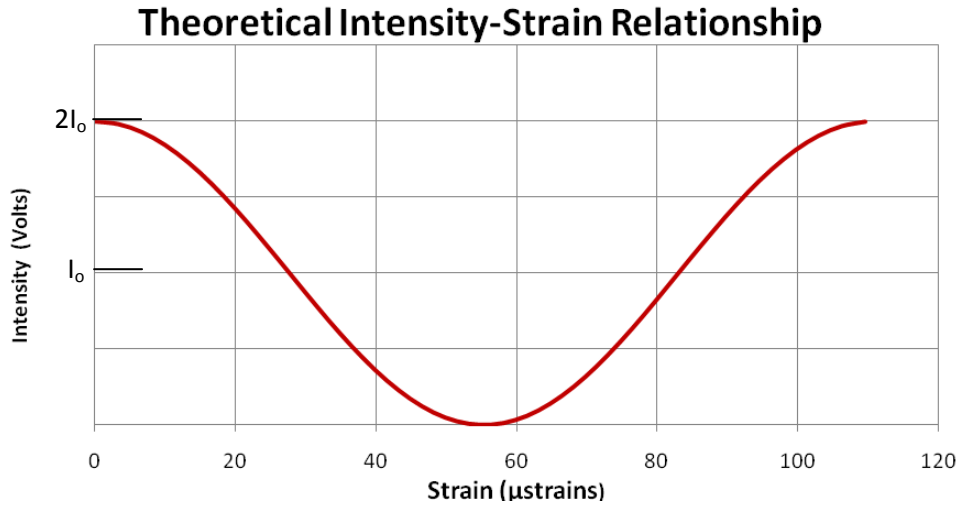

Figure 21 Theoretical Relationship Between a Given Intensity and its Corresponding Strain

From the graph in Figure 21, it is clear that as the strain increases, the intensity follows a sinusoidal pattern. Consequently, to determine the exact strain value the number of waves, or

fringes, needs to be counted. To avoid fringe counting in this experiment, the applied load was calculated for the cantilever beam to remain within one fringe.

A one fringe variation corresponds to at change in phase of 2π. As a result, equation 3.13 can be used to solve for the strain at one fringe variation, which can be substituted in the original strain equation given by equation 3.11. Rearranging this equation allows us to determine the maximum theoretical applied force for one fringe variation, seen in equation 3.15. Remaining within one fringe avoids fringe counting to determine the strain. The maximum applied force is related to the wavelength, λ, the thickness of the beam, t, the width of the beam, b, Young's modulus, E, the length of the cavity sensing region, L_{cavity} , the length of the beam, L, and the distance from the center of the beam, c. A detailed, step by step, calculation can be seen in Appendix D.

$$F_{maximum} = \frac{\lambda b\, t^3 E}{12 L L_{cavity}\, c} \tag{3.15}$$

When calculating the maximum force, it was assumed that the fiber was laid perfectly along the surface of the beam, at a value of *c* equal to exactly half of the thickness. Calibration would compensate for uncertainties in the placement of the fiber inside the groove. A maximum applied force of 160.0 grams was calculated to remain within one fringe variation, the calculation is shown in Appendix E.

3.3.2 Computational Modeling

Finite element Analysis was also performed to determine the location of maximum strain when the beam was statically loaded. Finite Element Analysis is a method of modeling complex structures by dividing the structure in elements. Integration and Partial Differential Equations are used to determine the response of the system under various conditions. This system can be utilized to determine the maximum strain on the cantilever beam.

The cantilever was designed from three components, a beam that was fixed between an upper and lower block clamping system as shown in Figure 22 below. The block was made from Aluminum 6061 and the beam would be of Aluminum 6063-T5. Also, the beam would have a small 1.5875 mm groove to lay the sensor that would extend 25.4 mm from the fixed end of the beam. To ensure the PVC fiber covering could fit through the block, the upper block had a matching groove to provide the appropriate tolerances.

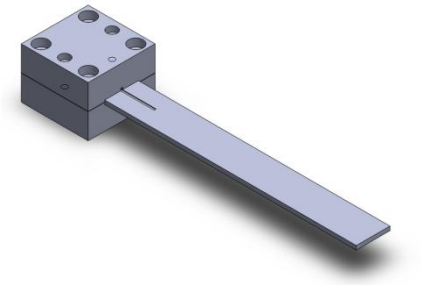

Figure 22 Cantilever Design

The cantilever was manufactured to be attached to a piezoelectric shaker using four countersunk 0.25 inch corner through holes shown in Figure 22. The two, smaller #8-32 holes were used to secure the upper block to the lower block.

Finite Element Analysis of this model was done using SolidWorks Simulation. SolidWorks Simulation is an add on to the SolidWorks interface that lets the user directly test CAD models, including modal, stress, impact, and heat analysis among many others (Simulation , 2010). The load was applied at the end of the beam. The beam was constrained assuming perfect boundary conditions. Therefore, the face where the beam meets the block was fixed in all directions. Also, the surface of the countersunk holes was fixed in all directions because this was the location where the screws would be locking the cantilever into the piezoelectric shaker. A 4-point Jacobian, fine mesh was applied to the beam. The results are shown in Figure 23

below and validate the analytical computations with the maximum strain located along the surface of the fixed end of the beam.

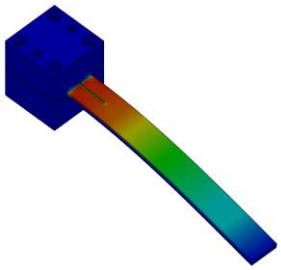

Figure 23 Finite Element Model-Cantilever Beam

3.3.3 System Setup

A hanger system was employed at the end of the cantilever beam to statically apply the load in increments of the 5 grams. Each of the weights used were weighted on a calibrated scale to ten-thousands of a gram accuracy. The opto-mechanical setup was used to measure the output light intensity from the FPI and was recorded using the virtual instrument (VI) from the LabView program shown in Figure 24. A 16-bit data acquisition (DAQ) system from National Instruments, model USB 6229-BNC, was used to read the output from the photodetector.

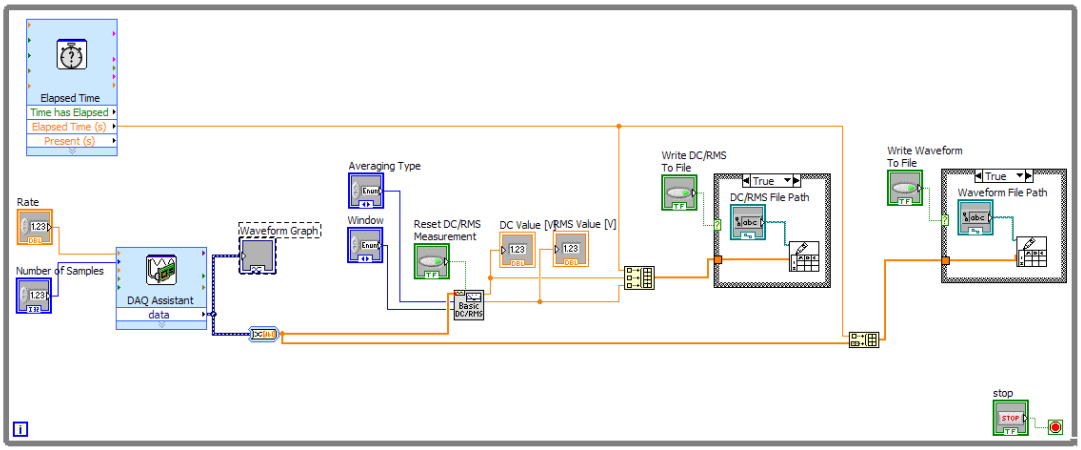

Figure 24 Static VI Block Diagram

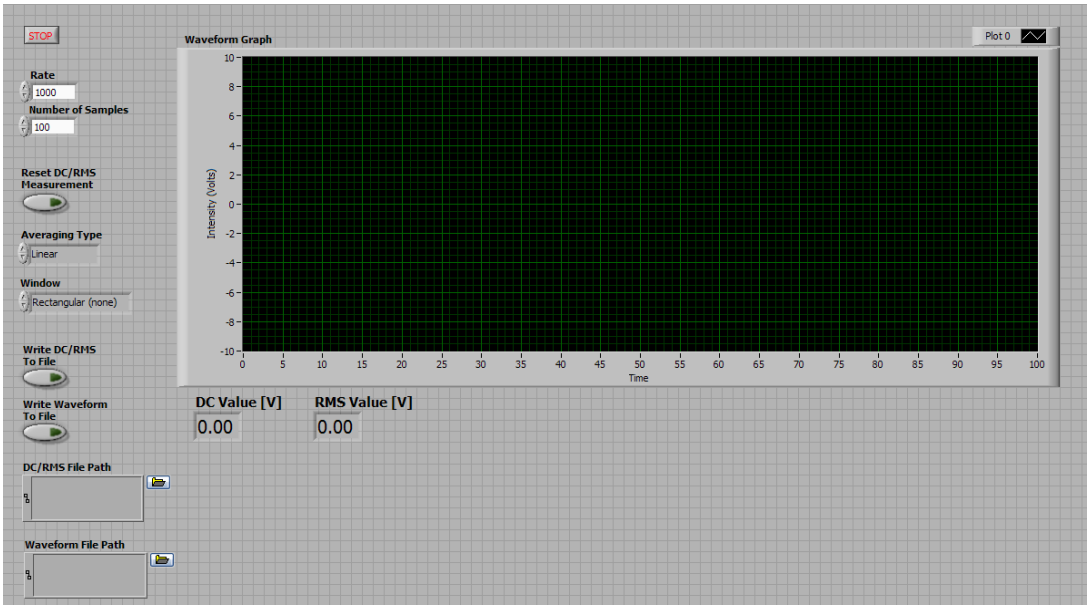

Figure 25 Static VI Front Panel

The block diagram shown in Figure 24 was built to record the output voltage as a function of time. Controls were made so that the number of samples and sampling rate could be controlled on the DAQ system. The output voltage is sent to a waveform graph and also to a "Basic DC/RMS" function. This function allows the user to view the DC value and the root mean square (RMS) value from the magnitude of the inputs. Data from both the waveform graph and the DC/RMS values were sent to a respective build array and written to a file that could be specified. The Front panel, user interface, of this VI can be seen in Figure 25.

The results from the static load testing would give the resolution of the of the FPI system in microstrains per millivolt, equation 3.16. The inverse of this number will determine the gage factor, which can be compared to a typical strain gage, equation 3.17. Additionally, by examining the resolution of the DAQ system, the lowest measurable value of strain can be calculated and compared to that of typical strain gauges using the same resolution DAQ system.

$$Resolution = \frac{\Delta V}{\Delta \varepsilon} = \frac{V_2 - V_1}{\varepsilon_2 - \varepsilon_1} \quad (3.16)$$

$$Gauge\ Factor = \frac{\Delta \varepsilon}{\Delta v} \quad (3.17)$$

3.4 Dynamic Evaluation

Dynamic testing was done on two components. The first was using the manufactured cantilever beam that was used for static testing. Additionally, another FPI was attached to a scale model wind turbine blade at location where the blade is fixed to the block, which is the area of maximum strain. The scale model of the blade is shown below in Figure 26 and was rapid prototyped using a plastic polymer. The blade had an overall length of 100 mm. The hole pattern was also designed to fit into a model EV-30 piezoelectric shaker.

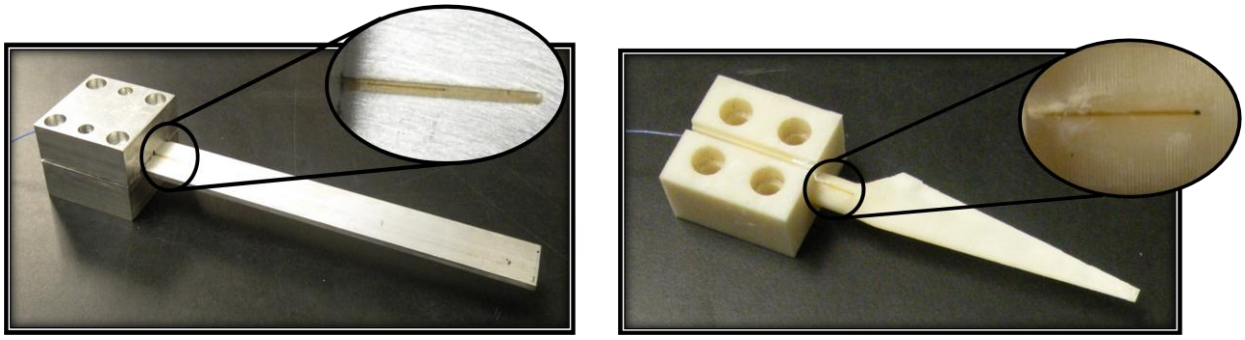

Figure 26 Cantilever Beam and Wind Turbine Blade with FPI attached

3.4.1 Analytical Calculations

The modes of vibration for the cantilever could be calculated using equation 3.18, where C_n is a constant given based on which mode is being determined, E is young's modulus, I_{zz} is the moment of inertia about the *z-axis*, $\ddot{m}$ is the mass per unit length, and L is the length of the beam. Table 3.1 shows the natural frequency of the beam for the first three bending modes of the beam. Detailed calculations are shown in Appendix F. The natural frequency of the block was also calculated to ensure that the beam and block did not have a close natural frequency. The natural frequency for the block can be seen in Appendix G.

$$\omega_n = \frac{C_n}{2\pi}\sqrt{\frac{EI_{zz}}{\ddot{m}L^4}} \tag{3.18}$$

Mode of Vibration	C_n value	Natural Frequency
1st Bending	3.516	68 Hz
2nd Bending	22.0345	426.16 Hz
3rd Bending	61.6972	1193 Hz

Figure 27 Cantilever Beam Modes of Vibration

Analytical calculations were not done on the turbine blade because of the complicated geometry. Hand calculations could have large error, which would affect the interpretation of the results.

3.4.2 Computational Calculations

The first three bending modes for the cantilever beam and the wind turbine blade were determined from finite element modeling. The young's modulus used was 68.9 GPa for both aluminum 6061 and aluminum 6063-T5. Figure 28 shows the results and an exaggerated view of the mode shape for each bending. The beam was fixed at the bottom of the figure and red signifies maximum displacement, which is at the free end of the beam. Blue represents zero displacement. Ideal boundary conditions show that there should no displacement at the fixed end of the wall. For each additional bending mode there is an additional node where no displacement occurs. For the cantilever beam, the first three bending modes were at 68.75 hz, 430.3 Hz, and 1205 Hz, respectively.

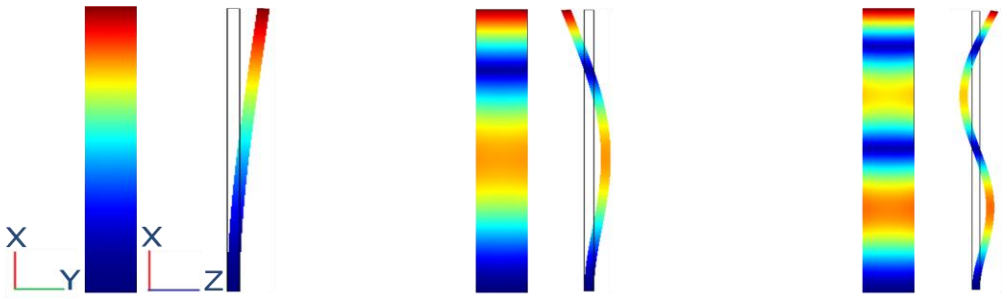

Figure 28 Cantilever Beam Bending Modes

The first three bending modes are shown for the scale model of the wind turbine blade in Figure 29. The same color distributed is used for the displacement of the blade, where blue represents no displacement and red represents maximum displace. The exact properties of the plastic used to make the prototype of the blade were unknown for this analysis. As a result, a young's modulus value of 15.5 GPa was used based research in general plastic properties. The boundary conditions are at the base of the blade, corresponding to the bottom of the models shown in Figure 29. The first three bending modes for the wind turbine blade were 175.6 Hz, 534.3 Hz, and 1136.69 Hz, respectively.

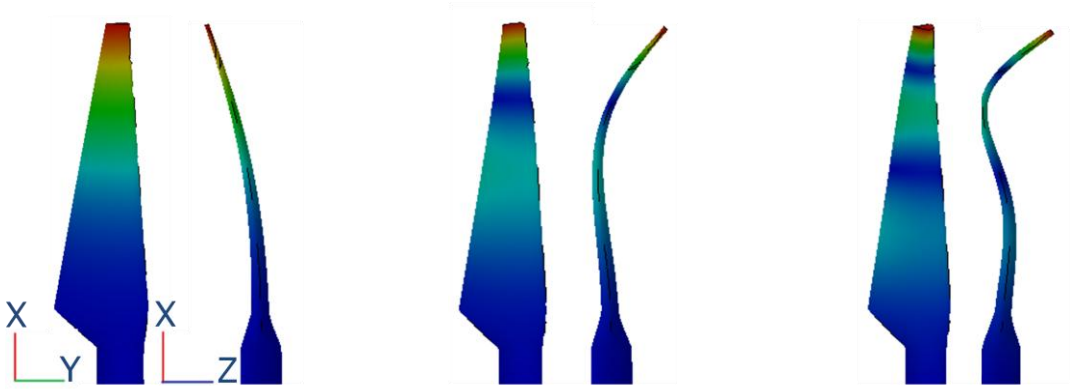

Figure 29 Scaled Wind Turbine Blade Bending Modes

3.4.3 Dynamic System Setup

The same opto-mechanical setup was used in the dynamic testing of the turbine blade and the cantilever beam. A EV-30 piezoelectric shaker was mounted vertically and excited using a function generation, and amplifier. The basic components of the piezoelectric system can be seen in Figure 30 below. The blade and the cantilever beam were interchanged during each test. The fiber optic cable was connected to our opto-mechancial setup.

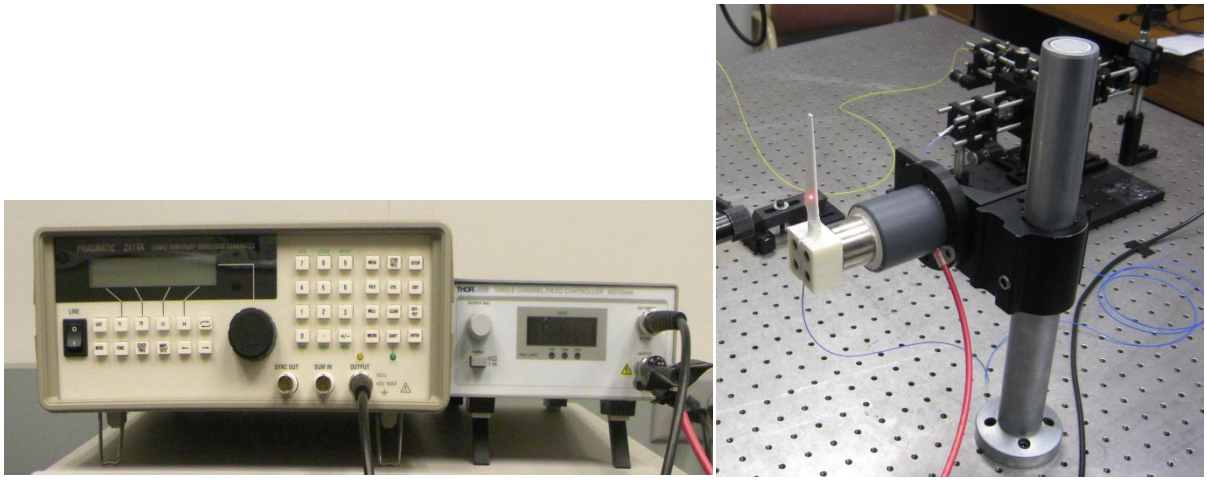

Figure 30 Dynamic Testing setup

This setup was connected to the DAQ system and the data was analyzed using another VI that is shown below. The VI for this system was combined to collect data from two systems. The first was from the FPI sensor and the second from the Laser Vibrometer system that is described in the next section. The main components of the system are the time domain graph and the power spectrum graph. The time domain graph shows the input light intensity as a function of time for the FPI and shows the displacement of the beam for the vibrometer. The power spectrum graph identifies the natural frequency for each system. In addition, there are controls that output the maximum light intensity of the FPI and the maximum beam or blade

deflection for the vibrometer. The combination of the two systems allows for a direct comparison of two methods of comparing the natural frequency. The block diagram of this system and the corresponding front panels can be seen in Figure 31, Figure 32, Figure 33 on the proceeding pages. The VI's also have the capabilities to record the data to files.

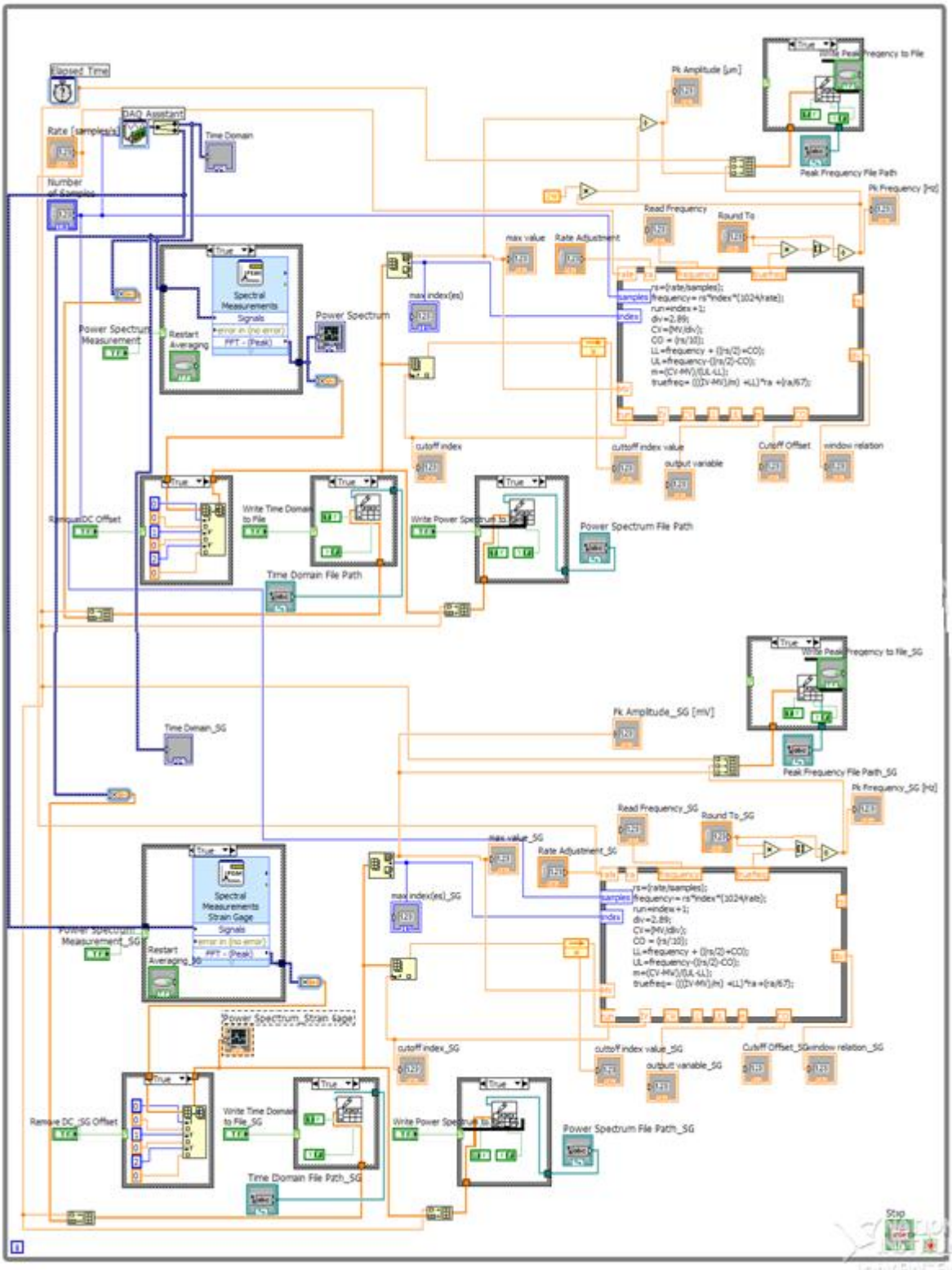

Figure 31 Dyanamic VI for FPI and Vibrometer Block Diagram

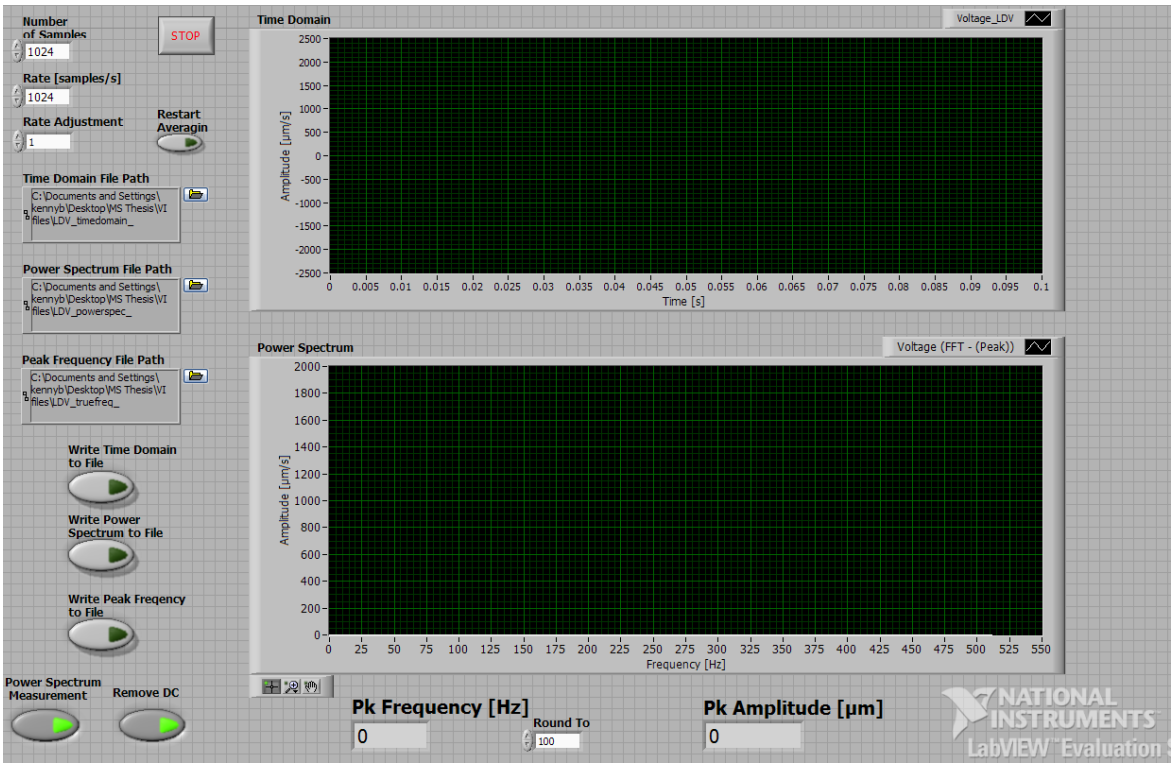

Figure 32 Front Panel: Vibrometer

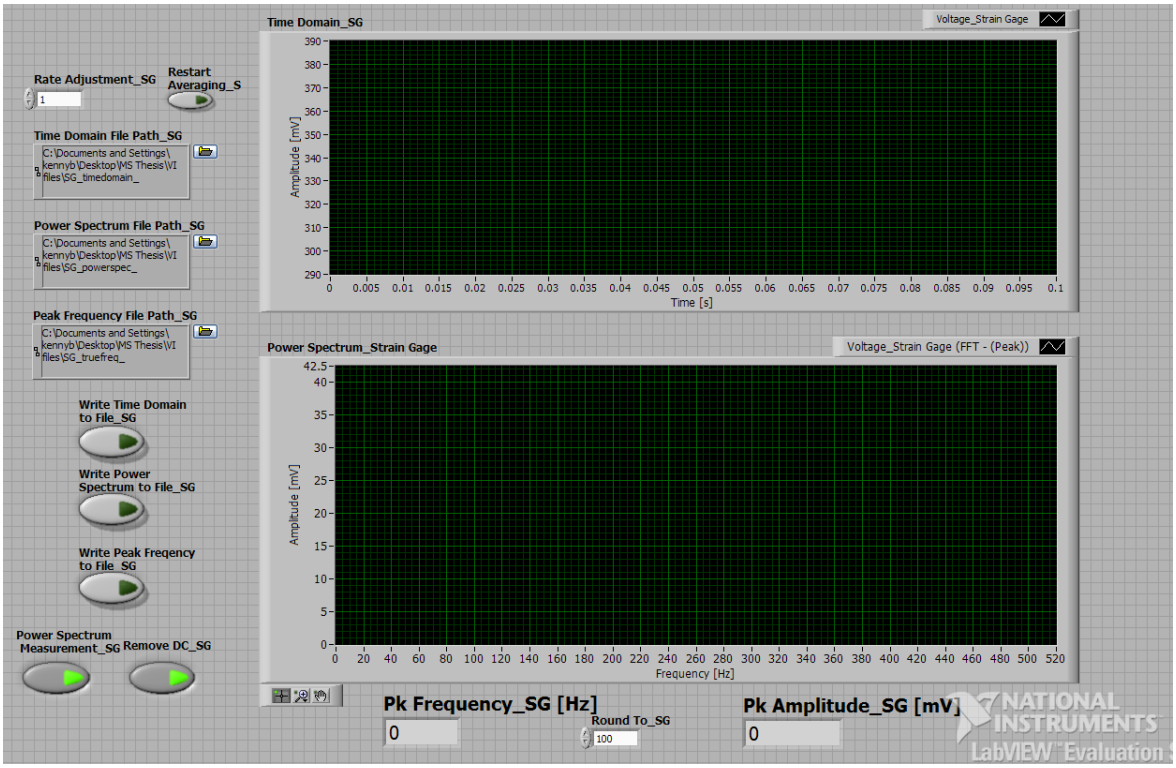

Figure 33 Front Panel FPI

3.4.4 Laser Vibrometry

The natural frequency of each component was calculated by a high resolution method called Laser Vibrometry. This method focuses a laser on the surface of interest, in our case the cantilever beam or wind turbine blade. An example of the setup is shown in Figure 34. The system used was from Polytec model number OFV 1000 Fiber Vibrometer. The principles of Laser Vibrometry utilize a two beam system. The phase shift of the laser that is focused on the component is compared to another reference beam. Therefore, the amplitude of the displacement and the natural frequency of the component can be determined (Laser Doppler Vibrometry, 2010).

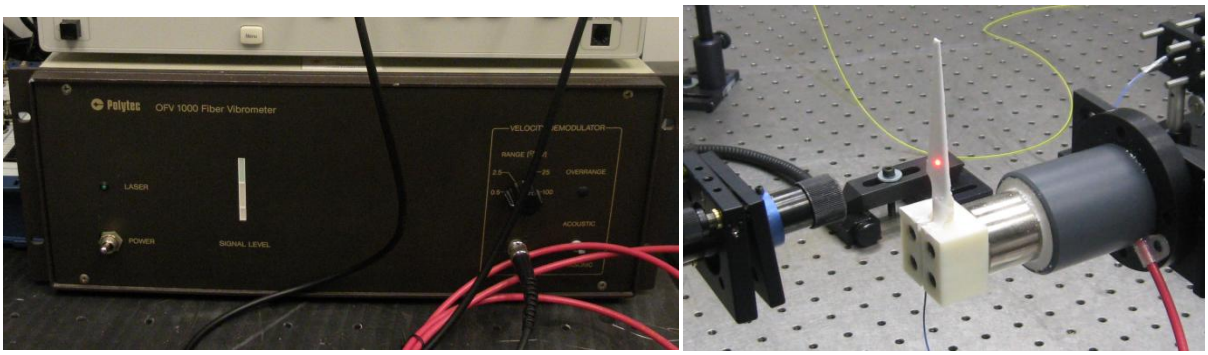

Figure 34 Laser Vibrometry

3.4.5 Time- Averaged Holographic Interferometry

Another high resolution technique was used to measure the natural frequencies of each of the components called Time-Averaged Holographic Interferometry. Holographic Interferometry is a method of measuring displacement on the order of a wavelength. A high resolution camera is used to determine the modulation of the component by combined an object and reference beam. (Vest, 1979). The amplitude and phase of the light is reconstructed and a frozen image is

reproduced using dark and light fringes. The fringes represent deflections in the component, but do not provide information on the direction of the displacement (Vest, 1979).

4 Results

The system was successful calibrated and the high resolution of the FPI was validated experimentally when compared to the analytical solutions, computational solutions and the other high resolution methods including Laser Vibrometry and Time-Averaged Holographic Interferometry.

4.1 Calibration Results

The calibrated system can be seen in the voltage-strain graph shown in Figure 35. The theoretically predicted relationship is shown in the graph.

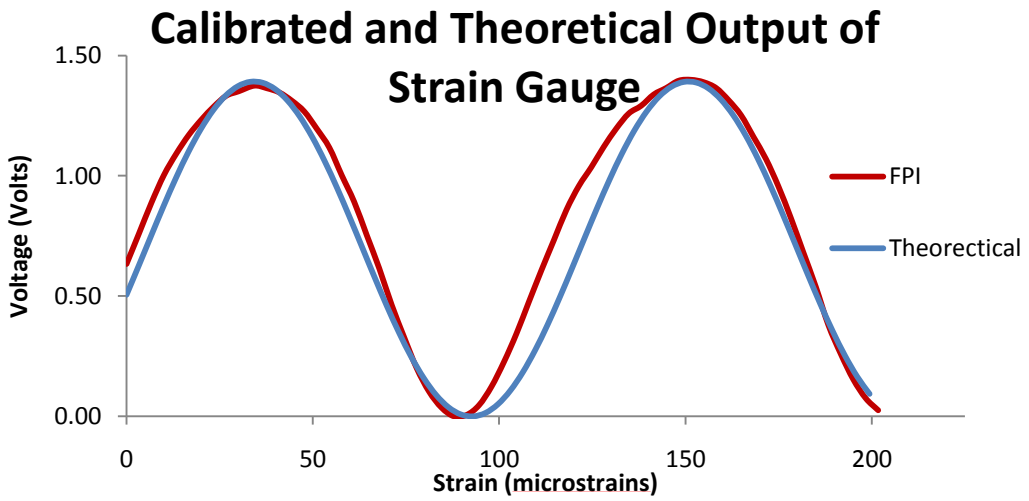

Figure 35 Comparison Between Experimentally Calibrated Output and Theoretically Expected Output

The FPI strain gage was calculated to have a gage factor of 47.48 mV/με. When examining the resolution of the 16 bit data acquisition system, it was calculated that the FPI sensor could measure a minimum strain value of approximately 6.4 nanostrains. This is equivalent to 6400 thousandths of a microstrain. These values were compared to those previously researched data for typical strain gauges. Strain gauges have a gauge factor typically

of approximately 2.1 and can measure a minimum strain on the order of one microstrains, as previously mentioned.

Stability was a key component for a successful static test. As weights were applied to the system, data was only recorded when the vibrations subsided and the system seemed constant. Yet, some hysterics in our system could have caused slight deviations, including acoustics from others talking nearby and vibrations from equipment on the nearby table. With the high resolution and measuring capabilities of our system, these influences cannot be ignored.

The uncertainty of our system was calculated to show that our calibrated system is within the expected values. The uncertainty in terms of the strain versus the applied force is shown below. The experimental data falls directly between the maximum and minimum values. The detailed uncertainty analysis can be seen in Appendix H.

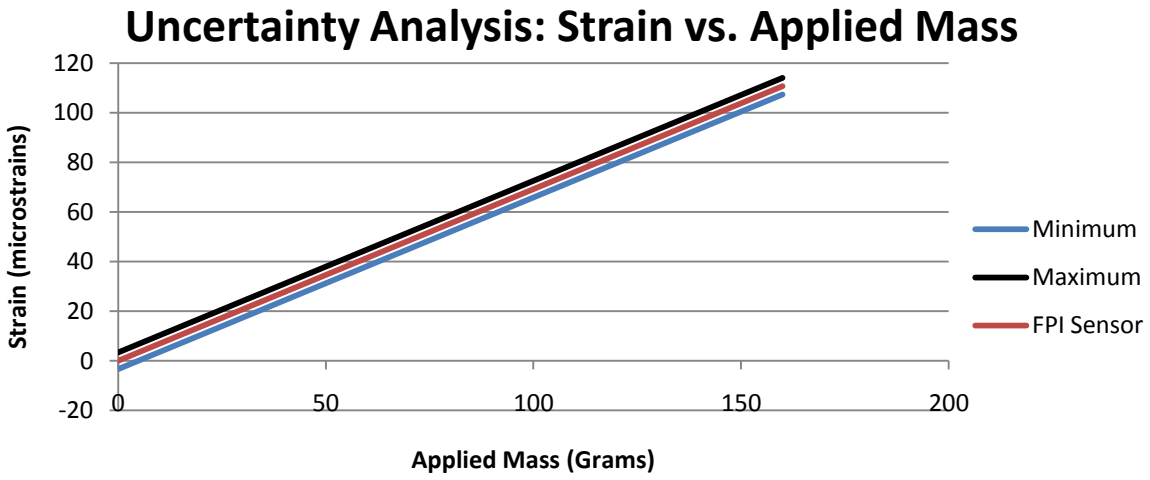

Figure 36 Uncertainty Analysis of Strain versus Applied Mass

4.2 Dynamic Testing Results

The proceeding sections examine the results for the dynamic testing of both the cantilever beam and the wind turbine blade.

4.2.1 Cantilever Beam Dynamic Results

The results for the first three bending modes of the cantilever beam analytically, computationally and experimentally with our FPI sensor, Laser Vibrometer and Holographic Interferometer, are summarized in below in Figure 37. Calculations on the average deviation of the FPI sensor from the other methods were conducted. Results showed an average deviation of 3.1 percent.

	1st Bending	2nd Bending	3rd Bending
Analytical	68 Hz	426.2 Hz	1193 Hz
Computational	68.75 Hz	430.3 Hz	1205 Hz
FPI Sensor	65.1 Hz	420.2 Hz	1190 Hz
Vibrometer	65.71 Hz	420.2 Hz	1190 Hz
Holography	65.61 Hz	414.9 Hz	1168 Hz

Figure 37 Dynamic Analytical, Computational and Experimental Comparison – Cantilever Beam

The results were also plotted showing the natural frequency and the corresponding bending mode for each method. The graph verifies the close relationship between all methods and the high measuring capabilities of the FPI sensor. In addition, the holographic pictures are compared alongside the Finite Element Solution, shown in Figure 38.

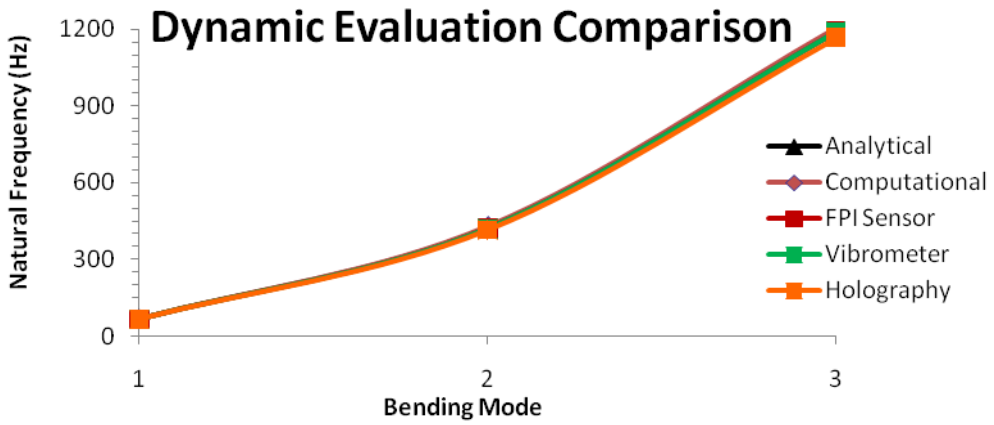

Figure 38 Cantilever Beam Natural Frequency Comparison

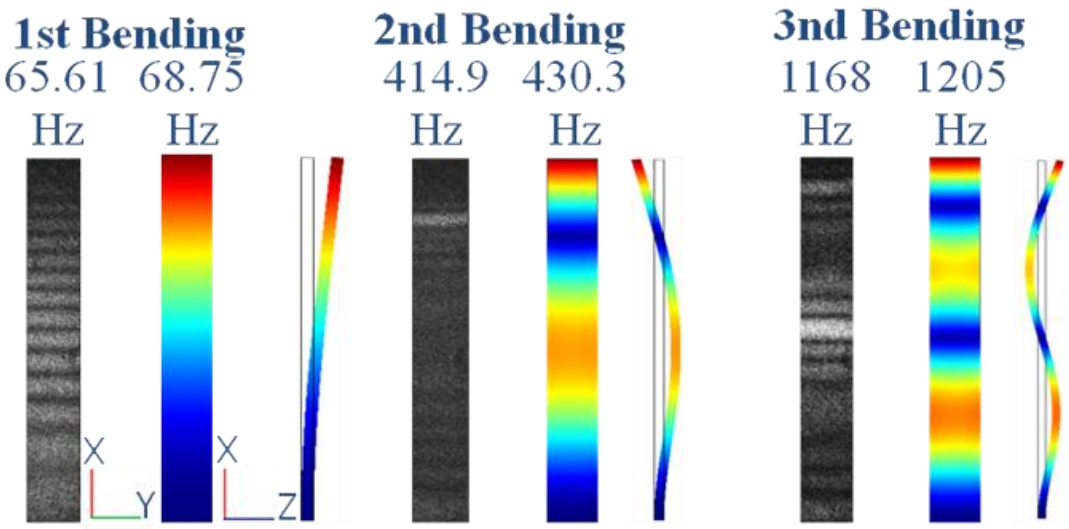

Figure 39 Cantilever Beam – Holographic vs. FEM Results

The Holographic images produced from the cantilever beam have poor contrast because of the size of the beam. The beam had to be a greater distance from the light source to capture the entire component, which means less light was able to be captured by the camera. Also, the displacements in the beam were so large at lower frequencies that the exposure time had of the camera had to be high enough to capture deflection while still making sure that the pixels in the image were not saturated. This balance in camera exposure time also made it difficult to produce higher quality holographic images.

The Finite Element solutions provided the greatest deviation from the experimental results because perfect boundary conditions were assumed for the analysis. In actuality, the clamping mechanism in our cantilever beam was most likely a source of error. Yet, all of the experimental data, including Laser Vibrometry and Time Averaged Holography, showed much smaller deviation from the FPI sensor.

4.2.2 Wind Turbine Blade Dynamic Results

The dynamic testing results for the wind turbine blade show similar, high accuracy results in the experimental data. Figure 40 summarizes the results for the computational calculation, experimental result, Laser Vibrometry, and Time Averaged Holographic Interferometry. The average deviation was calculated to be 1.6 percent.

	1st Bending	2nd Bending	3rd Bending
Computational	175.6 Hz	534.3 Hz	1136.69 Hz
FPI Sensor	180.76 Hz	540.58 Hz	1145.25 Hz
Vibrometer	180.84 Hz	540.49 Hz	1145.25 Hz
Holography	176.62 Hz	538.4 Hz	1134.2 Hz

Figure 40 Dynamic Analytical, Computational and Experimental Comparison – Scaled Wind Turbine Blade

The results were again plotted showing the natural frequency at each of the bending modes for the wind turbine blade in Figure 41 below. Once again, the holographic solutions are shown against the Finite Element Solutions in Figure 42. The high measuring capabilities of the system were again validated by comparing the results of the FPI sensor.

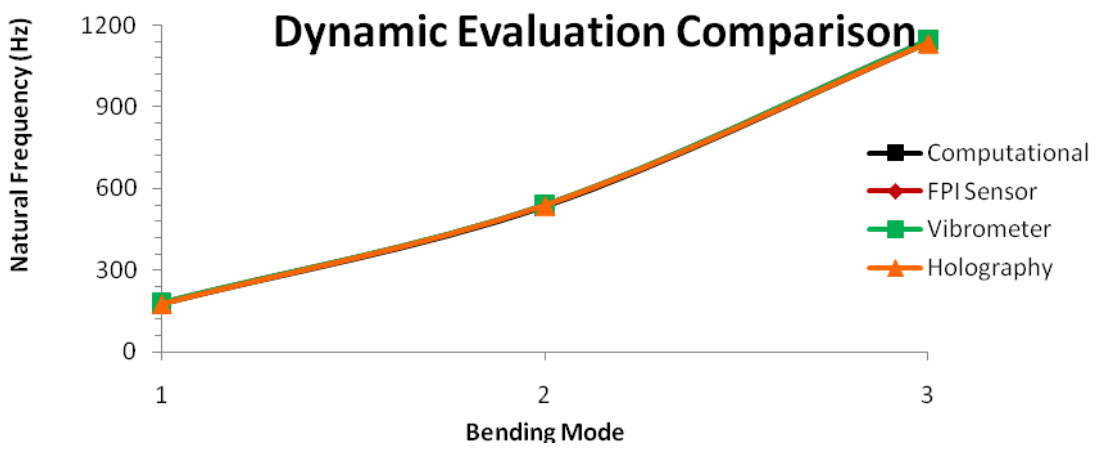

Figure 41 Turbine Blade Natural Frequency Comparison

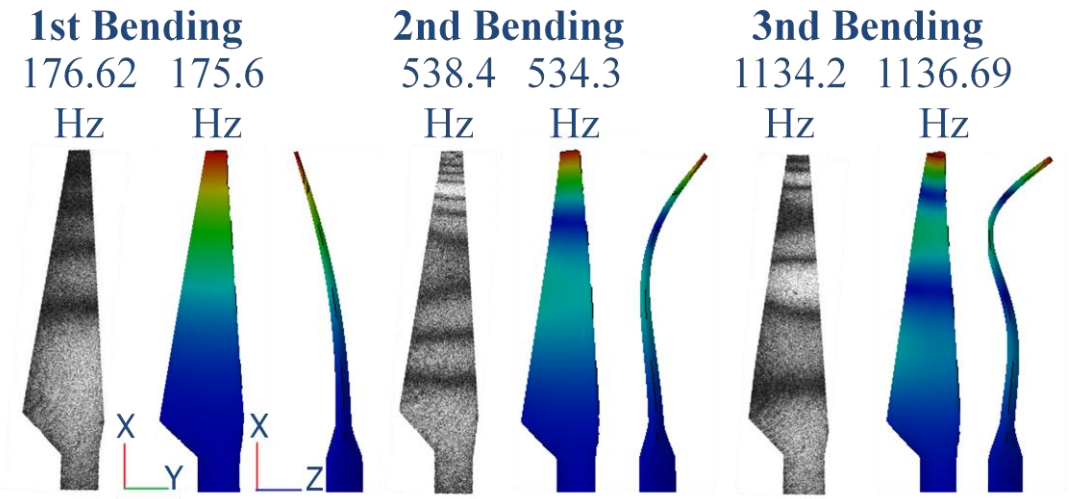

Figure 42 Scaled Wind Turbine Blade – Holographic vs. FEM Results

The Holographic images for the wind turbine blade produced higher contrast images because the size of the blade. The nodes can be seen in each of the Holographic images and directly correspond to the Finite Element Solutions. There were some variations in the FEM and the experimental results because the prototype machine did not have the tolerance capabilities necessary to reproduce the model exactly as expected.

5 Conclusions

A new generation fiber optic strain sensor was successfully identified, calibrated, and applied to simulate potential real world applications. Comparisons between the fiber optic sensor and a typical foil strain gauge proved the FPI was superior in aspects including immunity to electromagnetic waves and resolution. In additional, the size of the optical fiber provides a non-invasive design on the order of 125 micrometers in diameter that can be attached to the surface of the materials or embedded directly in the material.

Fiber optic sensors are the future of sensors as the world pushes to miniaturize opto-electrical components. FPI sensors have the high measuring capabilities and size to detect the small levels strains that may be experienced in these components. Similarly, these sensors are perfect for applications in wind turbine blades where they may be subjected to storms and electromagnetic interference. Other potential applications could be to components in MRI systems, which also cannot use typical foil gauges.

One of the major benefits of fiber optics is that they provide health monitoring capabilities on systems where typical foil gauges are not applicable. Therefore, this reduces down time maintenance on new generation equipment and, using the example of wind turbines, could generate higher volumes of energy over time. This is the next generation sensing system for a world moving towards energy independence and a cleaner environment.

6 Future Work

Future testing should be done on this sensor to evaluate its performance and durability under different environmental conditions. Wind turbine blades are subjected to extreme temperatures, high winds, and precipitation, all of which should be examined. Once further testing has been completed, the FPI should be attached to a full scale model of a wind turbine blade. A health monitoring system could be developed where an alarm system alters engineers when the turbine blade is subjected to high strains that could potentially damage the blade or minimize the blades lifespan. Systems of FPI sensors could be incorporated into a variety of structural applications to create a type of nervous system that can detect damages, strains, and provide information on the health of the structure.

7 References

Analog Devices, Inc. (2010). *ADXL202 - Inertial Sensors*. Retrieved April 20, 2010, from Analog Devices: http://www.analog.com/en/sensors/inertial-sensors/adxl202/products/product.html

Analog Devices, Inc. (1999). *Low Cost 62 g/610 g Dual Axis iMEMS® Accelerometers with Digital Output.* Retrieved April 20, 2010, from Analog Devices: http://www.analog.com/static/imported-files/data_sheets/ADXL202_210.pdf

Anolog Devices, Inc. (2010). *MEMS: Inertial Measurments Units, High g Accelerometers, Low g Accelerometers*. Retrieved April 15, 2010, from Analog Devices: http://www.analog.com/en/mems/products/index.html

Belleville, C., & Duplain, G. (1993). White-light interferometric multimode fiber-optic strain sensor. *Optics Letters , 18* (1), 78-80.

Dimension Engineering. (2010). *A Beginner's Guide to Accelerometers*. Retrieved January 18, 2010, from www.dimensionengineering.com

FBGS Technologies. (2009). Retrieved November 12, 2009, from www.fbgs-technologies.com

FISO Technologies Inc. (2010). Retrieved January 21, 2010, from www.fiso.com

Furlong, C. (2010, April 17). Strain Gages, Bridge Output and Calibration. Worcester, MA: Worcester Polytechnic Institute.

Gangopadhyay, T. K. (2004). Prospects for Fibre Bragg Gratings and Fabry-Perot Interferometers in Fibre-Optic Vibration Sensing. *Sensors and Actuators A Physical* , 20-38.

Huston, T. D., Ambrose, T., & Barker, D. (1994). *Intelligent Civil Structures Activites in Vermont* (Vol. 3.2).

Jodon. (2010). Retrieved April 28, 2010, from www.jodon.com

Laser Doppler Vibrometry. (2010, April 6). Retrieved April 12, 2010, from Wikipedia: http://en.wikipedia.org/wiki/Laser_Doppler_vibrometer

Measures, R. M. (2001). *Structural Monitoring with Fiber Optic Technology.* San Diego, CA: Academic Press.

Merzbacher, C., Kersey, A., & Friebele, E. (1995). Fiber Optic Sensors in Concrete Structures: A Review. 196-208.

National Instruments. (2010). Retrieved April 12, 2010, from www.ni.com

Olympus. (2010). Retrieved April 28, 2010, from www.olympus.com

Polytec. (2010). Retrieved April 27, 2010, from www.polytec.com

Pragmatic. (2010). Retrieved April 27, 2010, from www.pragmatic.com

Qwick Connect. (1999). The Secret Life of Fiber. *Glenair , 6* (3), 1-4.

Simulation . (2010). Retrieved 3 24, 2010, from SolidWorks: http://www.solidworks.com/sw/products/fea-cfd-simulation-sofware.htm

Sutherland, H., & Mandell, J. (2004). Effect of Mean Stress on the Damage of Wind Turbine Blades. *Journal of Solar Energy Engineering* , 126.

ThorLabs. (2010). Retrieved April 28, 2010, from www.thorlabs.com

Vest, C. (1979). *Holographic Interferometry.* New York: John Wiley & Sons.

Widas, P. (1997). *Introduction to Finite Element Analysis.* Blacksburg: Virginia Tech Material Science and Engineering.

Yin, S., Yu, F. T., & Ruffin, P. B. (2008). *Fiber Optic Sensors* (Second ed.). Boca Raton, FL: CRC Press Taylor & Francis Group.

Appendix A: MathCAD for Analytical FEA Calculations

Calculations for Spring Constants

k is the equivalent spring constant
A is the cross sectional area of the object
E is the elastic modulus
L is the length of the material

General Spring Constant Equation

$$k = \frac{A * E}{L}$$

Material Properties:

For Pure Silica Glass:

$$E_g = \frac{71700N}{mm^2}$$

$$A_g = 0.01169mm^2$$

For Fusion Weld (Pure Silica Glass):

$$E_w = \frac{71700N}{mm^2}$$

$$A_w = 0.0146mm^2$$

L varies for each element

Global

Solve for the equivalent spring stiffness of the global system

Element 1:

$$L_1 = 0.2422mm$$

Fusion Weld at Element 1

$$k_1 = \frac{A_w * E_w}{L_1}$$

Glass at Element 1

$$k_{1g} = \frac{A_g * E_g}{L_1}$$

Element 2:

$$L_2 = 2.2195mm$$

NO Fusion Weld at Element 2

Glass at Element 2

$$k_{2g} = \frac{A_g E_g}{L_2}$$

Element 3:

$$L_3 = 0.1228mm$$

Fusion Weld at Element 3

$$k_3 = \frac{A_w E_w}{L_3}$$

Glass at Element 3

$$k_{3g} = \frac{A_g E_g}{L_3}$$

Element 4:

$$L_4 = 0.1228mm$$

NO Fusion Weld at Element 4

Glass at Element 4

$$k_{4g} = \frac{A_g E_g}{L_4}$$

Element 5:

$$L_5 = 0.1306mm$$

Fusion Weld at Element 5

$$k_5 = \frac{A_w E_w}{L_5}$$

Glass at Element 5

$$k_{5g} = \frac{A_g E_g}{L_5}$$

Calculate the equivalent spring constants for the individual spring constants of the elements in parallel.

Element 1: $k_{eq\,1} = k_1 + k_{1g}$

Element 2: $k_{eq\,2} = k_{2g}$

Element 3: $k_{eq\,3} = k_3 + k_{3g}$

Element 4: $k_{eq\,4} = k_{4g}$

Element 5: $k_{eq\,5} = k_5 + k_{5g}$

Calculate the equivalent spring constant for the elements in series in order to find the total equivalent spring constant.

$$k_{eq,total} = \frac{1}{\left[\left(\frac{1}{k_{eq\,1}}\right) + \left(\frac{1}{k_{eq\,2}}\right) + \left(\frac{1}{k_{eq\,3}}\right) + \left(\frac{1}{k_{eq\,4}}\right) + \left(\frac{1}{k_{eq\,5}}\right)\right]}$$

Calculate the total displacement.

$$Force: P = 4.002 * 10^{-3} N$$

$$Displacement: u = \left(\frac{P}{k_{eq,total}}\right)$$

Local

Solve for the nodal displacements using the matrix equation for linear springs.

$$f_n^e = force\ of\ element\ 'n'\ closest\ to\ node\ 'n'$$

Element 1: $\begin{bmatrix} k_{eq\,1} & -k_{eq\,1} \\ -k_{eq\,1} & k_{eq\,1} \end{bmatrix} * \begin{pmatrix} u_1 \\ u_2 \end{pmatrix} = \begin{pmatrix} f_1^1 \\ f_2^1 \end{pmatrix}$

Element 2: $\begin{bmatrix} k_{eq\,2} & -k_{eq\,2} \\ -k_{eq\,2} & k_{eq\,2} \end{bmatrix} * \begin{pmatrix} u_2 \\ u_3 \end{pmatrix} = \begin{pmatrix} f_2^2 \\ f_3^2 \end{pmatrix}$

Element 3: $\begin{bmatrix} k_{eq3} & -k_{eq3} \\ -k_{eq3} & k_{eq3} \end{bmatrix} * \begin{pmatrix} u_3 \\ u_4 \end{pmatrix} = \begin{pmatrix} f_3^3 \\ f_4^3 \end{pmatrix}$

Element 4: $\begin{bmatrix} k_{eq4} & -k_{eq4} \\ -k_{eq4} & k_{eq4} \end{bmatrix} * \begin{pmatrix} u_4 \\ u_5 \end{pmatrix} = \begin{pmatrix} f_4^4 \\ f_5^4 \end{pmatrix}$

Element 5: $\begin{bmatrix} k_{eq5} & -k_{eq5} \\ -k_{eq5} & k_{eq5} \end{bmatrix} * \begin{pmatrix} u_5 \\ u_6 \end{pmatrix} = \begin{pmatrix} f_5^5 \\ f_6^5 \end{pmatrix}$

Form Global Stiffness Matrix

$$\begin{pmatrix} k_{eq1} & -k_{eq1} & 0 & 0 & 0 & 0 \\ -k_{eq1} & (k_{eq1}+k_{eq2}) & -k_{eq2} & 0 & 0 & 0 \\ 0 & -k_{eq2} & (k_{eq2}+k_{eq3}) & -k_{eq3} & 0 & 0 \\ 0 & 0 & -k_{eq3} & (k_{eq3}+k_{eq4}) & -k_4 & 0 \\ 0 & 0 & 0 & -k_4 & (k_{eq4}+k_{eq5}) & -k_5 \\ 0 & 0 & 0 & 0 & -k_5 & k_5 \end{pmatrix} * \begin{pmatrix} u_1 \\ u_2 \\ u_3 \\ u_4 \\ u_5 \\ u_6 \end{pmatrix} = \begin{pmatrix} F_1 \\ F_2 \\ F_3 \\ F_4 \\ F_5 \\ P \end{pmatrix}$$

F_1, F_2, F_3, F_4, F_5 are equal to zero because there is no external force on those nodes
Set up equations in order to solve for nodal displacements: u_1 to u_6

$$F_1 = (k_{eq1} * u_1)$$
$$F_2 = (k_{eq1} + k_{eq2}) * u_1 - (k_{eq2} * u_3)$$
$$F_3 = (-k_{eq2} * u_2) + (k_{eq2} + k_{eq3}) * u_3 - (k_{eq3} * u_4)$$
$$F_4 = (-k_{eq3} * u_3) + (k_{eq3} + k_{eq4}) * u_4 - (k_{eq4} * u_5)$$
$$F_5 = (-k_{eq4} * u_4) + (k_{eq4} + k_{eq5}) * u_{35} - (k_{eq5} * u_6)$$
$$P = (-k_{eq5} * u_5) + (k_{eq5} * u_6)$$

Assume: $F_1, F_2, F_3, F_4, F_5 = 0$

Guess values of each nodal displacement and then use MathCAD to find the nodal displacements.

$$u_1 = 0nm$$
$$u_2 = 0.5142nm$$
$$u_3 = 11.11nm$$
$$u_4 = 11.37nm$$
$$u_5 = 34.2nm$$
$$u_6 = 34.48nm$$

Appendix B: List of Equipment used in Opto-Mechanical Setup

Main Opto-Mechanical Setup Equiptment

ThorLabs Mini-Series Breadboard

To properly support our opto-mechanical setup we needed a secure plate (Figure 43) to put it on. This metallic plate was equipped with an array of ¼-20 holes so that our setup could be secured at various points (ThorLabs, 2010). For our purposes we used a mini-series 12’’x8” breadboard.

Figure 43 Mini-Series Breadboard

ThorLabs ITC-502 Laser Diode Controller

To use our pigtailed laser diode, we needed an ITC-502 laser diode controller (Figure 44) to provide the correct voltage, current, temperature, and frequency to the diode. This device accomplishes these things with the help of a proportional-integral-derivative (PID) controller, letting us choose how much power to supply to the laser diode (ThorLabs, 2010).

Figure 44 ITC-502 Laser Diode Controller

ThorLabs TCLDM9 Laser Cooler

The laser diode must be kept within a certain temperature range to keep it stable and in great operating condition. A TCLDM9 Laser Cooler (Figure 45) with the help of the ThorLabs ITC-502 Laser Diode Controller was used to accomplish this task (ThorLabs, 2010).

Figure 45 TCLDM9 Laser Cooler

ThorLabs LPS-830-FC Laser Diode

The pigtailed laser diode used for this project is the LPS-830-FC from ThorLabs Figure 46. It has an 830nm wavelength and runs on an average of 1mW of power (ThorLabs, 2010).

Figure 46 Pigtailed 830nm Laser Diode

ThorLabs Post, PH2-ST Post Holder, and BA2T2 Adjustable Mounting Base

The opto-mechanical setup is positioned at the same height vertically using ½" diameter precision ground stainless steel posts of varying heights with 8-32 removable stud in the top. The posts were placed into a PH2-ST Post Holder (Figure 47) which has a locking thumbscrew which helps lock the post into. The post holder is then attached to a BA2T2 base plate which is secured to the breadboard using ¼-20" cap screws (ThorLabs, 2010).

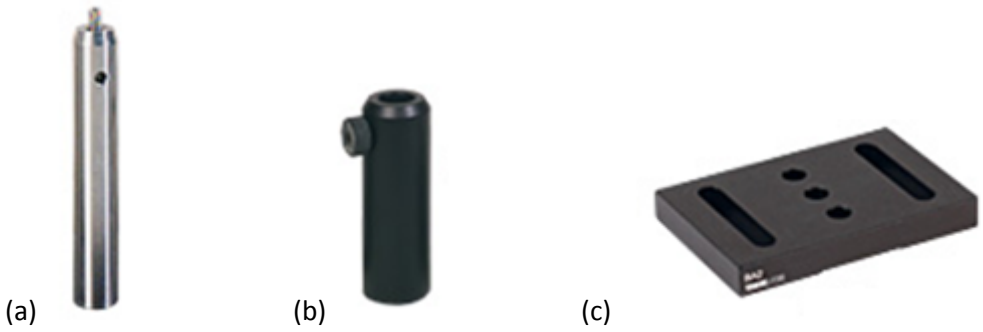

Figure 47 (a) Post, (b) Post Holder, (c) Mounting Base

ThorLabs 5mm Connecting Rods and Cage Plate

The entire opto-mechanical setup is arranged using ThorLabs 5mm connecting rods (Figure 48) in order to align and maintain structural rigidity of the setup. The individual components of the setup are attached to each other with the help of the 5mm rods. In addition to the components being attached to each other cage plates Figure 49 (ThorLabs, 2010).

Figure 48 Connecting Rod

Figure 49Connecting Plate

ThorLabs SM1FC FC Fiber Connector

The FC Fiber Connector (Figure 50), fixed to the end of the pigtailed laser diode is used to attach the output of the laser diode to the opto-mechanical setup (ThorLabs, 2010). This type of adaptor allows for quick change out of components if a problem occurs.

Figure 50 FC Fiber Adapter

ThorLabs SM1Z Z-axis Translator

To properly align the output of the pigtailed laser diode we needed a SM1Z (Figure 51) fitted with a SM1FC (ThorLabs, 2010). This Z-axis translator can adjust the distance between the output of the laser diode and the 20X objective lens at a micrometer level of precision.

Figure 51 SM1Z Z-axis Translator

Olympus 20X Objective Lens

The 20X objective lens (Figure 52) helped with the collimating and focusing of light (Olympus, 2010). Depending on the orientation of the lens in our opto-mechanical setup with respect to the incoming light because the light would either be collimated or focused into the next component of the setup.

Figure 52 Olympus 20X Objective Lens

ThorLabs ST1XY-D and HPT1 X-Y-axis Translator

The ST1XY (Figure 53) and (HPT1) (Figure 54) are the main components that aided us in the alignment of our opto-mechanical setup. Precision adjustments in both the X and Y-axis of the 20X objective lenses position were made using these translators (ThorLabs, 2010).

Figure 53 ST1XY-D X-Y-axis Translator

Figure 54 HPT1 X-Y-axis Translator

ThorLabs BS017 20mm Non-Polarized Beamsplitter Cube

The BS017 (Figure 55) is capable of splitting 700-1100nm light and is used to split the output of our project's 830nm laser diode with a 50:50 power ratio (ThorLabs, 2010). This beamsplitter cube effectively allows light to travel to the fiber Fabry-Perot Interferometer as well as to the detector in or experiments.

Figure 55 BS017 Beamsplitter Cube

ThorLabs CM1-4E Beamsplitter Cube Mount

We used the CM1-4ER (Figure 56) to mount the beamsplitter cube. This reusable cube mount is the center structure of the opto-mechanical setup and allows for other components to be screwed into it using the connecting rods (ThorLabs, 2010).

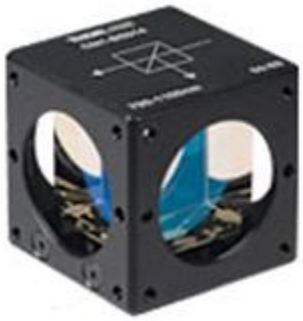

Figure 56 Beamsplitter Cube Mount

ThorLabs SM1ST Fiber Adapter

Connecting our fiber FPI sensor to the opto-mechanical setup required a SM1ST fiber adapter (Figure 57) fitted into a SM1Z Z-axis translator (ThorLabs, 2010). This fiber adapter allowed for quick and easy attachment of different fiber FPI sensors during our various experiments.

Figure 57 ST Fiber Adapter

FISO Technologies FOS-N-BA-C1-F1-M2-R1-ST Fabry-Perot Interferometer Strain Sensor

This new generation fiber optic strain sensor is the main component of our project. The FOS-N-BA-C1-F1-M2-R1-ST (Figure 58) is a 50µm multimode fiber Fabry-Perot Interferometer strain sensor that has an operating temperature of -40 °C to 250 °C, 20 mm bare tip, pyrocoated cable with 1 mm outer diameter, fiber length of 2 meters, ST fiber connector, and a sensing range of +/- 1000µe (FISO Technologies Inc., 2010). For a more in depth description of the sensor's principles of operation please refer to the background section.

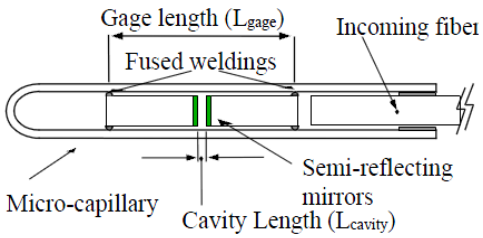

Figure 58 FOS-N-BA-C1-F1-M2-R1-ST Strain Sensor

ThorLabs DET10A High-Speed Photodetector

The final light output leaving the opto-mechanical setup is monitored using a DET10A high-speed photodetector (Figure 59). The battery operated DET10A is capable of detecting the small fluctuations in light intensity occurring in our experiments. It also has a single output which converts the light intensity measurements into a positive voltage using a terminating resistor (ThorLabs, 2010).

Figure 59 DET10A High-Speed Photodetector

National Instruments 16-Bit Data Acquisition System (DAQ)

The 16-Bit DAQ (Figure 60) was implemented to digitize the voltage output of the photodetector (National Instruments, 2010). The photodetector was connected to the DAQ via a BNC cable.

Figure 60 NI DAQ

Dell Core 2 Duo Computer Processor

To process all of the data from our experiments we utilized a generic computer processor.

Laser Vibrometer Setup Equipment

Jordon EV-30 Piezoelectric Shaker

The EV-30 Figure 61 is designed to excite or induce mechanical vibrations into test pieces at frequencies as high as several hundred kilohertz (Jodon, 2010). We needed this device

to non-destructively excite our cantilever beam and turbine scale model for our dynamic experiments.

Figure 61 Piezoelectric Shaker

Pragmatic 2414A 20MHz Arbitrary Waveform Generator

To control the operating frequency of the EV-30 piezoelectric shaker we needed a waveform generator. The Pragmatic 2414A Figure 62 allowed for specific frequencies as high as 20MHz to be generated so that we could analyze our cantilever beam and turbine blade scale model at their natural frequencies (Pragmatic, 2010).

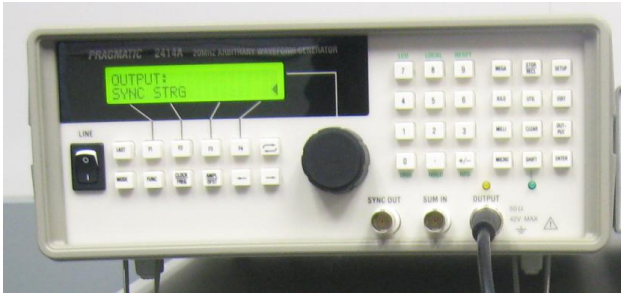

Figure 62 Pragmatic 2414A

Polytec OFV 1000 Fiber Vibrometer

The OFV 1000 Figure 63 is used to measure the displacement of an object as it is excited by a piezo electric shaker. A standard single-point measurement is used to determine the in-plane vibrations and displacements of the object such as a cantilever beam or a scale turbine blade

model. The laser beam from the vibrometer is split into one reference and one probe beam (Polytec, 2010). We used this device in our dynamic tests in order to have a comparison to our measurements taken by our FPI sensor.

Figure 63 Fiber Laser Vibrometer

ThorLabs MDT694A Single Channel Piezo Controller

The MDT694A Figure 64 combines precision control of the output voltage for maximum piezo resolution as well as a high output current capability which allows external modulation of the piezo (ThorLabs, 2010).

Figure 64 Single Channel Piezo-Controller

Appendix C: Force-strain Relationship

Summation of forces in the *x-direction* and *y-direction* as well as the moments gives the solutions given as follows based on the free body of the cantilever beam:

$R_x = 0$
$R_y = F$
$M = FL$

The relationship between the applied force and resulting strain was determined for the cantilever beam. The stress on the beam is equal to the moment multiplied by the distance from the center axis through the beam all divided by the moment of inertia of the beam.

$\sigma = \frac{Mc}{I_{zz}}$
$\varepsilon_{xx} = \frac{Mc}{I_{zz}E}$

The width of the base is defined by the variable, *b*, the thickness of the beam by the variable *t*.

$I_{zz} = \frac{1}{12}bt^3$

$\varepsilon_{xx}(F) = \frac{12FLc}{bt^3E}$

Appendix D : One Fringe Calculation

$$I = 2I_o[1 + \cos(\Delta\Phi)]$$

$$\Delta\Phi = K(\Delta L) = \frac{2\pi(\Delta L)}{\lambda}$$

$$\varepsilon_{xx} = \frac{\Delta L_{cavity}}{L_{cavity}}$$

$$\Delta L_{cavity} = \varepsilon_{xx} L_{cavity}$$

Substitute ΔL_{cavity} into to the $\Delta\Phi$ equation above and get the following equation:

$$\Delta\Phi = \frac{2\pi(\varepsilon_{xx} L_{cavity})}{\lambda}$$

For one Fringe, set delta phi to 2π and solve for the strain at 1 fringe:

$$\frac{2\pi(\varepsilon_{xx} L_{cavity})}{\lambda} = 2\pi$$

$$\varepsilon_{xx} = \frac{\lambda}{L_{cavity}}$$

Substitute the value for strain into the original equation for strain and force yields the final solution:

$$F_{maximum} = \frac{\lambda b t^3 E}{12 L L_{cavity} c}$$

Appendix E : Mass Calculation for One fringe

INPUT

$\lambda := 830 \cdot 10^{-9}$ Wavelength (meters)

$b := .0255$ Base (meters)

$t := .0030$ Thickness (meters)

$E := 68.9 \cdot 10^{9}$ Young's Modulus (Pa)

$L := .19$ Length of beam (meters)

$I_o := 1$ Intensity of Light

$i := 45$ Current (mA)

$c := .0015$ Distance equal to t/2 in Meters

$L_{cavity} := .00749$ Cavity length sensing region in Meters

SOLUTION

$$F_{maximum} := \left[\frac{\left(\lambda \cdot b \cdot t^3 \cdot E\right)}{12 \cdot L \cdot L_{cavity} \cdot c} \right] = 1.569831$$ Max. Force (Newtons)

$$m_{grams} := \frac{F_{maximum} \cdot 1000}{9.81} = 160.023592$$ Max. mass in grams

Knowing the maximum mass that can be applied to the end of the beam allows us to calculate the average intensity light output within the range.

$F_{min} := 0$

$F_{max} := 1.56983$

$\Delta F := .1$

$F := F_{min}, F_{min} + \Delta F .. F_{max}$

$$\varepsilon_{xx}(F) := \frac{(12 \cdot c \cdot L \cdot F)}{b \cdot t^3 \cdot E}$$

$\varepsilon_{xx}(1.569831) = 1.107109 \times 10^{-4}$

Appendix F: MathCAD Natural Frequency Calculations

INPUT All properties are given by Knovel.com selected material properties

$E := 68.9 10^{9}$ Young's Modulus (E) in Psi

$\rho := 270($ Density in kg per square meter

$C_n := 3.51($ Metric constant for natural frequency

$b := .0255$ Base in meters

$h := .0030$ Height in meters

$L := .19$ Length in meters

SOLUTION

$I_{zz} := \frac{(b \cdot h^3)}{12} = 5.975 \times 10^{-11}$ Moment of Inertia of the bar

$m := \rho \cdot b \cdot h = 0.209$ Mass per unit length of the beam

$w_{n1} := \frac{3.516}{2 \cdot \pi} \cdot \left[\sqrt{\frac{(E \cdot I_{zz})}{m \cdot L^4}} \right] = 68.001$ First Natural Frequency in Hz

$w_{n2} := \frac{22.0345}{(2 \cdot \pi)} \cdot \left[\sqrt{\frac{(E \cdot I_{zz})}{m \cdot L^4}} \right] = 426.155$ Second Natural Frequency in Hz

$w_{n3} := \frac{61.6972}{(2 \cdot \pi)} \cdot \left[\sqrt{\frac{(E \cdot I_{zz})}{m \cdot L^4}} \right] = 1.193 \times 10^{3}$ Third Natural Frequency in Hz

Appendix G : MathCAD – Natural Frequency of Block

INPUT All properties are given by Knovel.com selected material properties

Assumption: Although blocks are made from separate components, they act as one solid unit.

$b1 := .05$ Base in meters

$h1 := .05$ Height in meters

$L1 := .05$ Length in meters

SOLUTION

$I1 := \frac{\left(b1 \cdot h1^3\right)}{12} = 5.638 \times 10^{-7}$ Moment of Inertia of the bar

$m1 := \rho \cdot b1 \cdot h1 = 7.023$ Mass per unit length of the beam

$w_{nB} := C_n \cdot \left[\sqrt{\frac{(E \cdot I1)}{m1 \cdot L1^4}}\right] = 1.005 \times 10^5$ Natural Frequency in Hz

Appendix H : Uncertainty Analysis of Strain versus Applied Mass

INPUT

$t := .0030$

$\delta t := .00000$

$b := .0255$

$\delta b := .00000$

$L := .19$

$\delta L := .000$

$F := 1.5$

$\delta F := .000$

$E := 68.9 \cdot 10^{9}$

$\delta E := .$

$I_o := 1$

$\lambda := 830 \cdot 10^{-9}$

$\delta\lambda := 20 \cdot 10^{-9}$

$c := .00126$

$\delta c := 2.54 \times 10^{-4}$

$c := .0014$

$\delta c := .00000$

SOLUTION

$$\varepsilon_{xx} := \frac{(12 \cdot L \cdot c \cdot F)}{b \cdot t^3 \cdot E} = 1.064 \times 10^{-4}$$

$$\delta\varepsilon_{xx} := \left[\left[\delta L \cdot \frac{(12 \cdot c \cdot F)}{b \cdot t^3 \cdot E}\right]^2 + \left[\delta F \cdot \frac{(12 \cdot L \cdot c)}{b \cdot t^3 \cdot E}\right]^2 + \left[\delta b \cdot \frac{(-12 \cdot c \cdot F)}{b^2 \cdot t^3 \cdot E}\right]^2 + \left[\delta t \cdot \frac{(-36 \cdot c \cdot F)}{b \cdot t^4 \cdot E}\right]^2 + \left[\delta E \cdot \frac{(-12 \cdot c \cdot F)}{b \cdot t^3 \cdot E^2}\right]^2 + \left[\delta c \cdot \frac{(-12 \cdot F)}{b \cdot t^3 \cdot E}\right]^2\right]^{.5} = 3.358 \times 10^{-6}$$

$$\%d\varepsilon\delta L := \frac{\left[\delta L \cdot \frac{(12 \cdot c \cdot F)}{b \cdot t^3 \cdot E}\right]^2 \cdot 100}{\delta\varepsilon_{xx}^2} = 0.687$$

$$\%d\varepsilon\delta F := \frac{\left[\left[\delta F \cdot \frac{(12 \cdot L \cdot c)}{b \cdot t^3 \cdot E}\right]^2 \cdot 100\right]}{\delta\varepsilon_{xx}^2} = 0.01$$

$$\%d\varepsilon\delta b := \frac{\left[\left[\delta b \cdot \frac{(-12 \cdot c \cdot F)}{b^2 \cdot t^3 \cdot E}\right]^2 \cdot 100\right]}{\delta\varepsilon_{xx}^2} = 0.106$$

$$\%d\varepsilon\delta t := \frac{\left[\left[\delta t \cdot \frac{(-36 \cdot c \cdot F)}{b \cdot t^4 \cdot E}\right]^2 \cdot 100\right]}{\delta\varepsilon_{xx}^2} = 66.947$$

$$\%d\varepsilon\delta E := \frac{\left[\left[\delta E \cdot \frac{(-12 \cdot c \cdot F)}{b \cdot t^3 \cdot E^2}\right]^2 \cdot 100\right]}{\delta\varepsilon_{xx}^2} = 0$$

$$\%d\varepsilon\delta c := \frac{\left[\left[\delta c \cdot \frac{(-12 \cdot F)}{b \cdot t^3 \cdot E}\right]^2 \cdot 100\right]}{\delta\varepsilon_{xx}^2} = 32.25$$

$$\%check := \%d\varepsilon\delta L + \%d\varepsilon\delta F + \%d\varepsilon\delta b + \%d\varepsilon\delta t + \%d\varepsilon\delta E + \%d\varepsilon\delta c = 100$$